




The edges of galaxies: Tracing the limits of star formation

Nushkia Chamba¹, Ignacio Trujillo^{2,3}, and Johan H. Knapen^{2,3}

¹ The Oskar Klein Centre, Department of Astronomy, Stockholm University, AlbaNova, 10691 Stockholm, Sweden
 e-mail: nushkia.chamba@astro.su.se

² Instituto de Astrofísica de Canarias (IAC), 38205 La Laguna, Tenerife, Spain

³ Departamento de Astrofísica, Universidad de La Laguna (ULL), 38200 La Laguna, Tenerife, Spain

Received 22 March 2022 / Accepted 7 September 2022

ABSTRACT

The outskirts of galaxies have been studied from multiple perspectives for the past few decades. However, it is still unknown if all galaxies have clear-cut edges similar to everyday objects. We address this question by developing physically motivated criteria to define the edges of galaxies. Based on the gas density threshold required for star formation, we define the edge of a galaxy as the outermost radial location associated with a significant drop in either past or ongoing in situ star formation. We explore ~1000 low-inclination galaxies with a wide range in morphology (dwarfs to ellipticals) and stellar mass ($10^7 M_\odot < M_\star < 10^{12} M_\odot$). The location of the edges of these galaxies (R_{edge}) were visually identified as the outermost cutoff or truncation in their radial profiles using deep multi-band optical imaging from the IAC Stripe82 Legacy Project. We find this characteristic feature at the following mean stellar mass density, which varies with galaxy morphology: $2.9 \pm 0.10 M_\odot \text{pc}^{-2}$ for ellipticals, $1.1 \pm 0.04 M_\odot \text{pc}^{-2}$ for spirals, and $0.6 \pm 0.03 M_\odot \text{pc}^{-2}$ for present-day star-forming dwarfs. Additionally, we find that R_{edge} depends on its age (colour) where bluer galaxies have larger R_{edge} at a fixed stellar mass. The resulting stellar mass–size plane using R_{edge} as a physically motivated galaxy size measure has a very narrow intrinsic scatter ($\lesssim 0.06$ dex). These results highlight the importance of new deep imaging surveys to explore the growth of galaxies and trace the limits of star formation in their outskirts.

Key words. galaxies: fundamental parameters – galaxies: photometry – galaxies: formation – methods: data analysis – methods: observational – techniques: photometric

1. Introduction

Galaxies grow and evolve through two main channels: in situ star formation via the conversion of gas into stars and ex situ stellar and gas accretion via merging and interactive events with its neighbourhood (e.g., Toomre & Toomre 1972; White & Rees 1978; Efsthathiou & Silk 1983). While merging events are expected to happen predominantly in the most massive galaxies, current stellar mass growth via in situ star formation occurs in the majority of dwarfs and spiral galaxies, and it depends on the density of gas in these systems. In other words, stars can form in a galaxy as long as the density of gas surpasses a critical threshold (e.g., Quirk 1972; Fall & Efsthathiou 1980; Kennicutt 1989; Schaye 2004). The radial location of the ‘edge’ of star formation as defined by this critical gas density threshold in a galaxy is thus a physically meaningful way to study the growth and evolution of galaxies.

This idea has recently been proposed by Trujillo et al. (2020) and Chamba et al. (2020) as a new, physically motivated definition of galaxy size (see also Chamba 2020, for a historical review on galaxy size measures). To make this definition operative, in these studies, we specifically chose a stellar mass density of $1 M_\odot \text{pc}^{-2}$ as a proxy to locate the gas density threshold required for star formation in galaxies based on theoretical (e.g., Schaye 2004) and observational (e.g., Martínez-Lombilla et al. 2019) evidence. This statement is based on the abrupt drop in the ultra-violet radial profiles of two Milky-Way-like galaxies reported by Martínez-Lombilla et al. (2019) in the region where their stellar mass density profiles are truncated (at $1 M_\odot \text{pc}^{-2}$ after correcting for inclination). Consequently, the radial location of this isomass contour was used as a size measure (dubbed

R_1), which is uniquely associated with the visual location of the edges of galaxies. Trujillo et al. (2020) have recently shown that the resulting size–stellar mass relation over five orders of magnitude in stellar mass ($10^7 M_\odot < M_\star < 10^{12} M_\odot$) produced an extremely tight distribution, with an intrinsic scatter (i.e. 0.06 dex) three times smaller than when using the de Vaucouleurs (1948) effective radius, which is a popular measure for galaxy size defined as the radius that encloses half the total light of a galaxy. Furthermore, Chamba et al. (2020) show that, in contrast to the effective radius that depends on the concentration of light in galaxies, R_1 is a much better representation of the boundaries of galaxies to fairly compare the sizes of distinctive galaxy populations or morphologies whose light distributions are very different.

While the above results are very promising, the truncation at $1 M_\odot \text{pc}^{-2}$ has thus far only been observed at the edges of Milky-Way-like disk galaxies (Martínez-Lombilla et al. 2019). As the exact stellar mass surface density depends on the efficiency of transforming gas into stars, the fixed value at $1 M_\odot \text{pc}^{-2}$ cannot be assumed to hold for galaxies of other morphologies and/or stellar masses as well. For this reason, we seek to measure the star formation threshold and consequently the sizes of galaxies belonging to wide ranges in morphology, from dwarfs to elliptical galaxies, and stellar mass. As a proxy for our measurement, we searched for a change in slope, cutoff, or truncation in the radial stellar mass density profiles of the galaxies in our sample. The origin of truncations in the outer profiles of galaxies is an open question and several interesting scenarios have been proposed as to its connection with the evolution of galactic disks (see van der Kruit & Freeman 2011, for a review). However, there is growing evidence that truncations

are intimately linked to thresholds in star formation activity (Kennicutt 1989; Roškar et al. 2008; Elmegreen & Hunter 2017; Martínez-Lombilla et al. 2019). Therefore, searching for a truncated feature in the stellar mass density profiles of different types of galaxies is also a step towards addressing the origin of this signature.

This paper is organised as follows. We explain the meaning and concept of galaxy edges in broader terms in Sect. 2. The imaging data and sample selection is described in Sect. 3. The details of the methods used can be found in Sections 4 and 5. The results are shown in Sect. 6 and discussed in Sect. 7. Our main conclusions are presented in Sect. 8. We assume a standard Λ Cold Dark Matter cosmology with $\Omega_m = 0.3$, $\Omega_\Lambda = 0.7$ and $H_0 = 70 \text{ km s}^{-1} \text{ Mpc}^{-1}$.

2. An intuitive and physically motivated definition of the edge of a galaxy

In computer vision, the edge of an everyday object is detected where there is a sharp contrast or change in their properties such as brightness, colour, shape or texture (see the recent review by Jing et al. 2022). The location of these features are frequently used to define the object's size. Automatically segmenting or detecting the edges of light sources such as galaxies using astronomical images, however, is a nontrivial task (e.g., Haigh et al. 2021). But this issue can be addressed by developing physically motivated criteria and features to define the edges of galaxies. In this paper, we define the edge at the outermost radial location associated with a significant drop in either ongoing or past in situ star formation. Consequently, the light beyond the edge is mostly contributed by ex situ stars belonging to the stellar halo (Trujillo et al. 2020; Font et al. 2020; Huang et al. 2022 and see Trujillo et al. 2021, for a clear example). The above reasons make our definition of the edge of a galaxy intuitive to the broader concept of the edge of an object because it marks a transition in an inherent property (the in situ star formation) of the galaxy. Our definition also motivates the use of the edge as a physical measure to fairly represent and compare the sizes of all galaxies, and as a method to define the outer stellar halo (see Trujillo et al. 2020; Chamba et al. 2020; Chamba 2020).

There is now growing evidence in the literature which suggest that a change in slope or cutoff feature in the outskirts of a galaxy's radial profile, called a 'truncation', is indicative of a star formation threshold, that is to say a drop in in situ star formation (Kennicutt 1989; Roškar et al. 2008; Elmegreen & Hunter 2017; Martínez-Lombilla et al. 2019; Díaz-García et al. 2022). For this reason, we use the truncation as a signature of the edge. However, we prefer the term 'edge' over the classical 'truncation' because truncations were specifically characterised for edge-on Milky-Way-like galaxies by van der Kruit (1979) and van der Kruit & Searle (1981a,b) while we aim to study these features in low-inclination galaxies. We select low-inclination galaxies because there are only a few studies in the literature where their outskirts have been explored (e.g., Hunter et al. 2011; Peters et al. 2017; Watkins et al. 2022) and in smaller sample sizes than what we examine here (~ 1000 galaxies). Low-inclination galaxies are also less affected by scattered light due to the point spread function (PSF; e.g., Trujillo et al. 2001) compared to edge-on galaxies which makes these galaxies practically advantageous when studying the properties of their edges.

For clarity, we point out that our definition of the edge does not depend on when star formation occurred in the galaxy, whether it is ongoing or recent as in star-forming galaxies, or happened in the distant past as in elliptical galaxies. We are thus

capable of implementing our definition on galaxies that have varied evolutionary pathways and comparing them on equal footing. In short, we characterise the edges of different types of galaxies, from dwarfs to giants (Sect. 3), within a common physically motivated framework, that is say edges indicative of a current or past star formation threshold. And we study these edges as a function of galaxy morphology and stellar mass.

The criteria we use to identify edges for each morphological type is detailed in Sect. 5. As we explain in Sect. 5, we perform this task using a large variety of evidence, including the stellar mass density profile, colour radial profile and the multi-band optical images. The radial location we use as a signature of the edge will be called R_{edge} . Consequently, we use R_{edge} as a physically motivated measure of galaxy size. We determine the stellar mass density at that location ($\Sigma_\star(R_{\text{edge}})$) and study the resulting size and stellar mass density as a function of galaxy stellar mass and morphology, all at low redshift (Sect. 6). We then discuss the implications of our results on the formation and evolution of galaxies (Sect. 7).

3. Data and sample selection

3.1. Deep Stripe 82 Imaging

A deep and wide multi-band survey with sub-kiloparsec spatial resolution is necessary to resolve the edges of a large sample of low-inclination galaxies where mass densities are low and the scale of the feature is of the order of $\sim 1 \text{ kpc}$. The deep g - and r -band images of the IAC Stripe 82 Legacy Project¹ (Fliri & Trujillo 2016; Román & Trujillo 2018) is thus chosen for this work. The dataset is a co-added version of the Sloan Digital Sky Survey (SDSS; York et al. 2000) 'Stripe 82' (Jiang et al. 2008; Abazajian et al. 2009) that has been optimised for low surface brightness astronomy. The limiting depth in surface brightness of these images are $\mu_g = 29.1 \text{ mag arcsec}^{-2}$ and $\mu_r = 28.5 \text{ mag arcsec}^{-2}$, both measured as a 3σ fluctuation with respect to the background of the image in $10 \times 10 \text{ arcsec}^2$ boxes. Assuming a $\sim 1 \text{ arcsec}$ spatial resolution for SDSS imaging, we are capable of resolving structures down to $\sim 600 \text{ pc}$ at the median redshift of $z \sim 0.03$ in our sample. We also made use of the publicly available extended ($R \sim 8 \text{ arcmin}$) PSFs of the SDSS survey (Infante-Sainz et al. 2020).

We used the same sample of galaxies recently studied in Trujillo et al. (2020), namely elliptical (c0-E+ TType) and spiral (S0/a-Im TType) galaxies from Nair & Abraham (2010) and a low-mass sample of (dwarf) galaxies from Maraston et al. (2013) within the Stripe 82 footprint. This can be considered the parent sample in our analysis. Galaxies with contaminated outskirts due to very bright stars, Galactic cirrus structures or nearby companion/interacting objects were removed from the initially selected sample. The final parent sample consists of 1005 galaxies (279 ellipticals, 464 spirals and 262 dwarfs) with stellar masses between $10^7 M_\odot < M_\star < 10^{12} M_\odot$ and redshift $0.01 < z < 0.1$. See Trujillo et al. (2020) for more details.

The sample of late-type galaxies studied in Bakos & Trujillo (2012, hereafter B12) and Peters et al. (2017, hereafter P17) was also included (24 galaxies) to complement our investigation in two ways: 1) the galaxies from B12 are located at lower distances and are therefore at a higher spatial resolution: the median distance of galaxies in this sub-sample is 54.2 Mpc which corresponds to a spatial resolution of about $260 \text{ pc arcsec}^{-1}$. This implies that the edge (if any) should be more prominent for these

¹ <http://research.iac.es/proyecto/stripe82/>

galaxies, 2) the sample from P17 is interesting because we can study galaxies with low inclinations. Upon examination, three galaxies from the P17 sample, namely UGC 2319, UGC 2418 and NGC 7716 were removed due to heavy scattered light contamination from nearby bright stars.

In order to explore the effect of the inclination on the location of the truncation, we also selected an edge-on galaxy from Shinn (2018), UGC09138, with similar rotational velocity after inclination correction than other low-inclination galaxies in our sample (SDSS J001431.85-004415.26, NGC1090, SDSS J011050.82+001153.36, SDSS J031133.38-004434.50). These galaxies have rotational velocities corrected for inclination² between $135 \text{ km s}^{-1} < V_{\text{rot}} < 155 \text{ km s}^{-1}$. UGC 09138 is outside the footprint of Stripe82 so imaging in the g and r bands from the Sloan Digital Sky Survey (SDSS) DR12 were obtained instead using the SDSS mosaic tool³. Using SDSS images for this galaxy does not affect our analysis. Therefore, a total of 1027 galaxies was analysed in this work.

3.2. GALEX

As the near and far ultra-violet (NUV and FUV, respectively) imaging of galaxies from Galaxy Evolution Explorer (GALEX; Martin et al. 2005; Morrissey et al. 2007) are sensitive indicators of star formation, this data is an ideal way of tracing the connection between edges and a star formation threshold. While GALEX imaging is also well-suited for the goals of this work in terms of depth (the images used here have a surface brightness limit of $29.6 \pm 0.5 \text{ mag arcsec}^{-2}$ (3σ , 100 arcsec^2)), its lower spatial resolution ($FWHM \sim 4.5$ and 5.4 arcsec in the FUV and NUV respectively) makes it unfeasible to explore in detail the edges in our full sample. We thus only used GALEX imaging for a handful of nearby galaxies in our sample to illustrate our definition of the edge of a galaxy and how it can be located in low-inclination galaxies compared to edge-on configurations using optical data.

We retrieved intensity maps from the Guest Investigator Program (GI) and Medium Imaging Survey (MIS) with the longest exposure times for the same galaxies we selected to explore the effect of the inclination on the location of the edges (see Sect. 3.1). This includes edge-on galaxy UGC 09138 (GI4-016007 and GI6-026001), intermediately inclined galaxies SDSS J001431.85-004415.26 (MISGCSN-29100-0389), NGC 1090 (MISGCSN-18291-04090), SDSS J011050.82+001153.36 (GI6-060007 and MISWZS01-30939-0269) and a face-on galaxy SDSS J031133.38-004434.50 (MISGCSN-18648-04100). We followed Morrissey et al. (2007) to convert the intensity to AB magnitudes.

4. Methods

To derive accurate surface brightness profiles of galaxies, the first steps are to find the elliptical parameters (centre, axis ratio, and position angle) that best describe the galaxy outskirts and to estimate the background of the image. There are two main complications that make these procedures challenging. One is the masking of all sources in the vicinity of the galaxy in the image and the second is accounting for contamination from scattered light. All these image processing techniques and the mea-

surement of the ellipticity of our sample of galaxies have been previously presented in Trujillo et al. (2020) and summarised in Chamba et al. (2020). The main steps to derive the radial surface brightness, colour and stellar mass density profiles of galaxies are described below:

First, individual image stamps centred on each galaxy were created in the g and r -band with dimensions $600 \times 600 \text{ kpc}^2$ for the massive galaxies and $100 \times 100 \text{ kpc}^2$ for the dwarfs in their rest frame. The dimensions of these stamps are at least five times greater than the rest-frame sizes of galaxies in our sample which are important for an accurate background subtraction and masking.

Second, scattered light due to point sources in each image was removed using the PSFs developed by Infante-Sainz et al. (2020) for the SDSS survey. We used *Gaia* DR 1 (Gaia Collaboration 2016) to initialise the locations and brightnesses of stars. The normalised PSFs were scaled to match the brightnesses of stars with the *Gaia* filter $G < 17 \text{ mag}$ at their locations on the image using IMFIT (Erwin 2015).

Third, all other sources surrounding the galaxy of interest were masked using an automated source detection tool ‘Max-Tree Objects’ (MTO; Teeninga et al. 2016). We used the version developed in Haigh et al. (2021) who demonstrated the algorithm’s capabilities in detecting low surface brightness light compared to other tools in the literature.

Fourth, background values for each galaxy were estimated using the fully masked images. We selected all the pixels that remained undetected (i.e. without source light) from the MTO segmentation map and used those regions to compute the mean background value and the associated dispersion. The mean background value was then subtracted from the masked images. The background subtracted images are the ones used to derive radial profiles of galaxies.

Fifth, the centre, axis-ratio, and position angle of each galaxy was computed at the location of the $26 \text{ mag arcsec}^{-2}$ isophote in the g -band by fitting an ellipse to the spatial distribution of the pixels at this isophote. This isophote is close to a traditional definition of galaxy extension by Holmberg (1958) and its location provides an initial estimate of the global shape and size of the galaxy. We visually checked these parameters to ensure the ellipse follows the global shape of the galaxy in its outskirts.

Sixth, we fixed these elliptical parameters and used them to derive the radial surface brightness profiles in μ_g and μ_r . Flux was averaged over concentric elliptical annuli from the centre of the galaxy to 200 arcsec , which is well beyond the visual extent of the galaxies in our sample. In this way, we were able to verify that our background subtraction was performed accurately (see Sect. 5.3 in Trujillo et al. 2020, for details).

Seventh, the profiles of the spiral and dwarf galaxies are corrected for the inclination effect following the model developed in Trujillo et al. (2020, see their Sect. 5.2). And all profiles are corrected for redshift dimming as well as Galactic extinction, using the position of the galaxies in the sky as input to NED’s calculator⁴. The corrected μ_g and μ_r profiles are then used to compute the $g-r$ colour and stellar mass density Σ_\star profiles.

Eighth, the stellar mass density profile was computed using the mass-to-light ratio (M/L) versus colour relation prescribed by Roediger & Courteau (2015). Explicitly, for a given wavelength λ , the relevant equations are:

$$\log \Sigma_{\star, \lambda} = 0.4(m_{\text{abs}, \odot, \lambda} - \mu_\lambda) + \log (M/L)_\lambda + 8.629 \quad (1)$$

$$\log (M/L)_\lambda = m_\lambda \times (\text{colour}) + b_\lambda, \quad (2)$$

² Values obtained from the HyperLeda database (Makarov et al. 2014): <http://leda.univ-lyon1.fr/>

³ <http://dr12.sdss.org/mosaics/>

⁴ <https://ned.ipac.caltech.edu/forms/calculator.html>

where we use $\lambda = g$ as it is our deepest imaging dataset and the $g - r$ colour to calculate $(M/L)_g$, using $m_g = 2.029$ and $b_g = -0.984$ (see Table A1 in Roediger & Courteau 2015).

We then visually examined the derived surface brightness and stellar mass density profiles of the galaxies for their edge (a change in slope or cutoff in their radial profiles as discussed in the Introduction, Sect. 2 and detailed criteria are specified later in Sect. 5). We selected the radial location of this feature (R_{edge}) and determined the stellar mass density in that location ($\Sigma_*(R_{\text{edge}})$). We also measured the colour at the edge location using the $g - r$ profile of the galaxy. From this colour, we determined the age of the stellar population using the extended MILES library in the SDSS bands, assuming the Kroupa Universal IMF⁵ (Vazdekis et al. 2012). We used the MILES predictions for a metallicity $[M/H] = 0$ and -0.71 (e.g., Radburn-Smith et al. 2014). Low metallicities have been observed in the outskirts of galaxies with the wide stellar mass range we study here ($10^7 M_\odot < M_* < 10^{12} M_\odot$), from low mass spirals to massive ellipticals (see e.g., Neumann et al. 2021). Additionally, as reviewed in Elmegreen & Hunter (2017) and Crnojević (2017), it is well established that the metal-poor stellar populations of local dwarf galaxies are very similar to the outskirts of disk galaxies. Therefore, both the fixed metallicity values we use from MILES are well-motivated to estimate the age at R_{edge} (see also the recent work by Cardona-Barrero et al. 2022).

Finally, we quantified the uncertainties in R_{edge} and $\Sigma_*(R_{\text{edge}})$ from the main sources: 1) background estimation and subtraction 2) colour to stellar mass conversion and 3) the visual identification of the edge. We followed a similar approach to that described by Trujillo et al. (2020) for the treatment of the first two. Namely, we fixed the location of the edge and then followed how the radial profiles move by a random quantity prescribed by the dispersion in the measured background value per image and stellar mass estimate in our procedure. In other words, we followed how the inferred $\Sigma_*(R_{\text{edge}})$ changes due to our background and mass estimate if we fix R_{edge} and vice versa. The dispersion in the stellar mass comes from comparing the estimate from Eq. (1) and those published by Maraston et al. (2013). Details of this comparison is provided in the Appendix in Trujillo et al. (2020) and our uncertainty estimations for this work are provided in Sect. 6. To infer the third source of uncertainty, we used repeated identifications from our visualisation procedure and evaluated the dispersion in these measurements. We discuss the visualisation procedure in more detail in Sect. 5.1.

We did not attempt to correct the surface brightness profiles of the galaxies due to the effect of the PSF as the radial location of the edge remains unchanged (see for e.g., Trujillo & Fliri 2016). However, we point out that (in general) the PSF can affect the estimated stellar mass density at the location of the edge. When corrected for the PSF effect, the brightness of either the μ_g or μ_r radial profiles would decrease (this effect is clearly visible in Trujillo & Fliri 2016, as the galaxy explored in that paper is highly inclined). Consequently, this effect means that all of our $\Sigma_*(R_{\text{edge}})$ estimations are upper limits. Considering the low inclinations of the galaxies in our sample, however, we expect that the effect of the PSF will be very mild (see e.g., Trujillo et al. 2001). In the case of the IAC Stripe 82 survey, the shape of the PSF in the g and r band filters are very similar (see Infante-Sainz et al. 2020). This statement is also true for GALEX (see Figs. 9 and 10 in Morrissey et al. 2007). Given that the stellar mass density is a function of μ_g and the $g - r$ colour (Eqs. (1) and (2)), at least

at first order, the effect of the PSF can be neglected in the $g - r$ profile. We leave a more detailed analysis on the full effect of the PSF for future work.

5. Locating the edge of a galaxy

This section details the procedure and criteria used to locate the edges of galaxies (Sect. 5.1). We then further discuss how the manifestation of the edge in the profile is physically motivated based on our edge definition and criteria for each morphological type. The criteria used to identify the signature of the edge is discussed for late-type, spiral galaxies (Sect. 5.2), early-type, elliptical galaxies (Sect. 5.3) and dwarf galaxies (Sect. 5.4). Several examples of the edges identified in our sample for each galaxy type are also shown.

5.1. Visualisation procedure and criteria

The visualisation procedure of each galaxy and its profiles is illustrated as a flowchart in Fig. 1. As motivated in Sect. 2, the main criterion we use as a signature of the edge is the change in slope in the outermost region of the galaxy's radial profiles. For each galaxy, we first examined their stellar mass density profile $\Sigma_*(R)$ for the edge and marked the radial location R_{edge} . If we were unable to locate a signature for edge, we proceeded to examine the surface brightness profiles in g and r , followed by the $g - r$ colour profile and do the same.

In the case of the colour profile, the criteria we used as a signature of the edge depended on the morphology of the galaxy. For disk galaxies, we searched for the location of a sudden reddening in the outer part of the profile, indicative of the end of the star-forming disk (Sect. 5.2). For elliptical galaxies, we used the location of a sudden transition towards bluer $g - r$ colours in the profile, potentially related to an outer envelope which assembled more recently compared to the galaxy's (redder) central regions (Sect. 5.3). And for dwarf galaxies, the signature of the edge in the colour profile appeared either as a transition to bluer or redder outskirts, a reflection of the varied star formation histories possible in these galaxies (inside-out or outside-in, respectively). We show examples of all three morphological types in the subsections below.

Once an initial identification of the edge is made using the above criteria, we plotted an ellipse (the same used to derive the radial profiles) at R_{edge} on the galaxy image to check whether the outskirts of the galaxy are elliptically symmetric in 2D. We show an example in the top right side of the flowchart of a galaxy and the profiles with the identified edge. If the galaxy is symmetric, we saved all the relevant parameters in the edge, namely, R_{edge} , the colour and mass density at the edge.

If a galaxy did not show a similar feature in its profile as shown in the example or is not symmetric in the outskirts, we further examined the 2D image for contaminants such as bright stars, neighbouring galaxies or streams that could affect the structure of the profile if the automated masking did not adequately remove the contaminated regions in the image. We also show an example in the lower section of the flowchart of a galaxy that contains tidal-like features beyond the edge. The profiles of this particular galaxy and other difficult cases are shown in Appendix A. We then re-computed the radial profiles for the galaxy and re-examined the data to locate an edge. We do not report edges in cases where even an improvement in masking and profile derivation did not allow us to locate an edge in our analysis (37% of our full sample; details in the next section.).

⁵ <http://research.iac.es/proyecto/miles/pages/photometric-predictions-based-on-e-miles-seds.php>

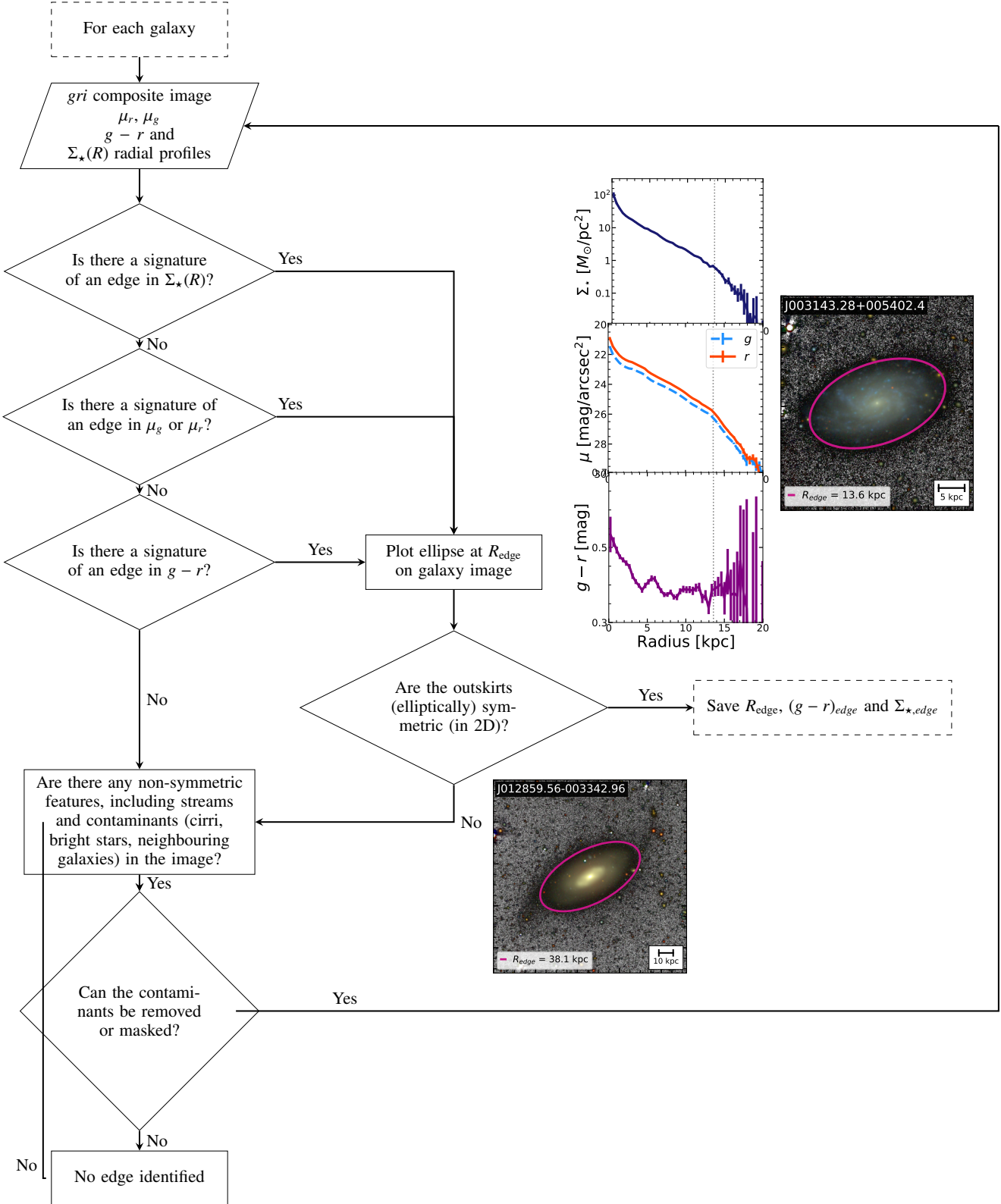


Fig. 1. Flowchart illustrating the visual identification of edges. An example of a galaxy, SDSS J003143.28+005402.4, and its profiles with the identified edge (vertical dotted line) is shown in the *top right side* of the flowchart. If the galaxy is symmetric, the relevant parameters in the edge, namely, R_{edge} , the colour and mass density at the edge are saved. However, if the galaxy contains any non-symmetric features such as tidal streams in its outskirts such as the example SDSS J012859.56–003342.96 shown in the *lower section* of the flowchart, they are masked and the process of finding the edge is attempted once again. No edges are reported for cases when even an improvement in the masking did not present an edge. See Sect. 5.1 for details.

Following the procedure detailed above, the edge for each galaxy was identified by the authors N. Chamba (NC) and I. Trujillo (IT). To quantify any dispersion in our inspections, we repeated our identifications and computed the average difference between these measurements. This quantity provides an estimate of the uncertainty in the visualisation of the edge.

We also show that our criteria and measurements are independent of the depth of the imaging used in Appendix B. The analysis is divided in two parts. In Appendix B.1, we examine a nearby (13.5 Mpc; Monelli & Trujillo 2019) disk galaxy with an edge, NGC1042, using deeper imaging from the LBT Imaging of Galactic Haloes and Tidal Structures (LIGHTS) Survey (Trujillo et al. 2021). We show that while deeper imaging allows one to characterise the edge with a higher signal-to-noise ratio, the edge of this galaxy may still be located with IAC Stripe 82 depth following our visualisation procedure. In Appendix B.2, we compare the surface brightness at which the edges of our parent sample appear with the limiting surface brightness of the IAC Stripe 82 images used. We show that all the edges studied in this work appear at surface brightnesses above the limiting depth of our data.

5.2. Dependence on orientation: Late-type galaxies

In the models studied by Martín-Navarro et al. (2014), the edge of a low-inclination Milky-Way-like galaxy with a bulge, disk and stellar halo appears as a very soft bump (or shallow change in slope) in the outer surface brightness profile while that of an edge-on galaxy of equal stellar mass appears prominently as a sharper cutoff. To complement this finding and visualise our definition of the edge, we show a few best case examples from our galaxy sample in Fig. 2 and how the appearance of the edge of a galaxy changes with orientation for real late-type galaxies with similar (inclination corrected) rotational velocities (see Sect. 3). For each galaxy, we show the IAC Stripe 82 *gri*-colour composite image with a pink contour marking the identified edge, *g* - *r*, GALEX NUV and FUV surface brightness profiles, *g* - *r* colour profile and resulting stellar mass density profile, Σ_* . The location of the edge is also marked in the panels as a dotted, grey vertical line.

Figure 2 shows that edges appear at the location where there is a change in slope in the outer part of the surface brightness profiles (mainly in the UV). This location corresponds to the region where the *g* - *r* colour rapidly becomes redder. The U-shape of colour profiles in disk galaxies were firstly identified in Bakos et al. (2008) and Azzollini et al. (2008). This sudden reddening in the outer part of the colour profile is indicative of both the significant drop in in situ star formation (as also confirmed by the truncation in the UV) and the emergence of the stellar halo component and/or stars migrated from the star-forming regions in the disk to the outskirts. We made use of this feature collectively as the criteria to identify the edge in the rest of our late-type, spiral galaxy sample.

The radial profiles of galaxies have been derived using elliptical annuli (Sect. 4). In Appendix C, we confirm that this method does not hinder our ability to identify the edges of low-inclination galaxies using their radial profiles compared to the method adopted for edge-on galaxies, that is to say using a slit through the galaxy's semi-major axis (see e.g., Martínez-Lombilla et al. 2019). We compare the ellipse and slit method for two galaxies: an edge-on case (UGC 09138) and a low-inclination one (NGC 1042) to study the effect of both these methods on galaxy orientation. We show that for UGC 09138, the elliptical annuli technique makes it unfeasible to locate the

edge while for NGC 1042 the location of the edge is possible with either method. Therefore, our identification of the edge for low-inclination galaxies is not hampered by the method we adopted to derive their radial profiles. We illustrate and explain the criteria we used to identify the edges of the elliptical and dwarf galaxies in our sample in the sections below.

5.3. The edges of early-type galaxies

Contrary to what happens in galaxies undergoing star formation, in the case of elliptical galaxies in our sample, their *g* - *r* radial profiles follow a similar global shape as shown in Fig. 3. The galaxies shown have a similar stellar mass $\sim 10^{11.5} M_\odot$. To locate their edges we have used a drastic change (a factor of five or higher difference in slope before and after the edge in the cases shown here) in colour in the outer parts of the system to mark a difference between the bulk of the object (with an homogeneous red colour) and potentially infalling (bluer) new material. Upon making this choice to mark the edge of these galaxies, we are implicitly assuming that the bulk of the elliptical galaxy was formed in an early burst and that the colour transition to the blue indicates the transition from the location of the original star formation radius to the outer envelope which was assembled (relatively) more recently.

5.4. The edges of dwarf galaxies

For the dwarf galaxies in Fig. 4, we find that the edge is visible in their *g* - *r* profiles and/or stellar mass density profile. These galaxies have a stellar mass $\sim 10^8 M_\odot$, and were chosen to illustrate the diversity in the colour radial profiles of dwarf galaxies which reflect their different morphology and substructure (see also the work by Herrmann et al. 2016). According to HyperLeda⁶ (Makarov et al. 2014), the morphology of these galaxies from case A to C labelled in the figure are Irr, Sd and SABd respectively. The *x*-axis of the radial profiles are scaled to the location of R_{edge} and the located edge is marked with the vertical black line. The edges of these galaxies occur at mass densities $\Sigma_*(R_{\text{edge}}) \lesssim 2 M_\odot \text{pc}^{-2}$. For clarity, we additionally explored case A using the semi-major axis method in Appendix C.1, confirming the R_{edge} identified as a change in slope in the radial profiles. In case B and C particularly, the edge marks the transition towards either bluer or redder outskirts. This observation could be related to inside-out or outside-in star formation in the dwarfs (e.g., Zhang et al. 2012). In a future paper, we explore the connection between the transition to redder or bluer outskirts in dwarf galaxies and galaxy environment (Chamba & Hayes, in prep.).

We identified the edges of the spirals, ellipticals and dwarfs in the rest of our sample following the physically motivated criteria described above. In summary, the signature of the edge of a galaxy may be identified as: a change in slope or cutoff in the radial surface brightness and/or stellar mass density profile (Sect. 2), a sudden reddening in the outer part of the colour profile for spiral galaxies, indicative of the end of the star-forming disk (Sect. 5.2), a sudden transition from red to blue colours for elliptical galaxies, to mark a difference between the core and recent infalling material, respectively (Sect. 5.3), or any of the above for dwarf galaxies. A transition to bluer or redder outskirts could reflect the inside-out or outside-in formation history, respectively (Sect. 5.4). We leave the exploration of alternative

⁶ <http://leda.univ-lyon1.fr/>

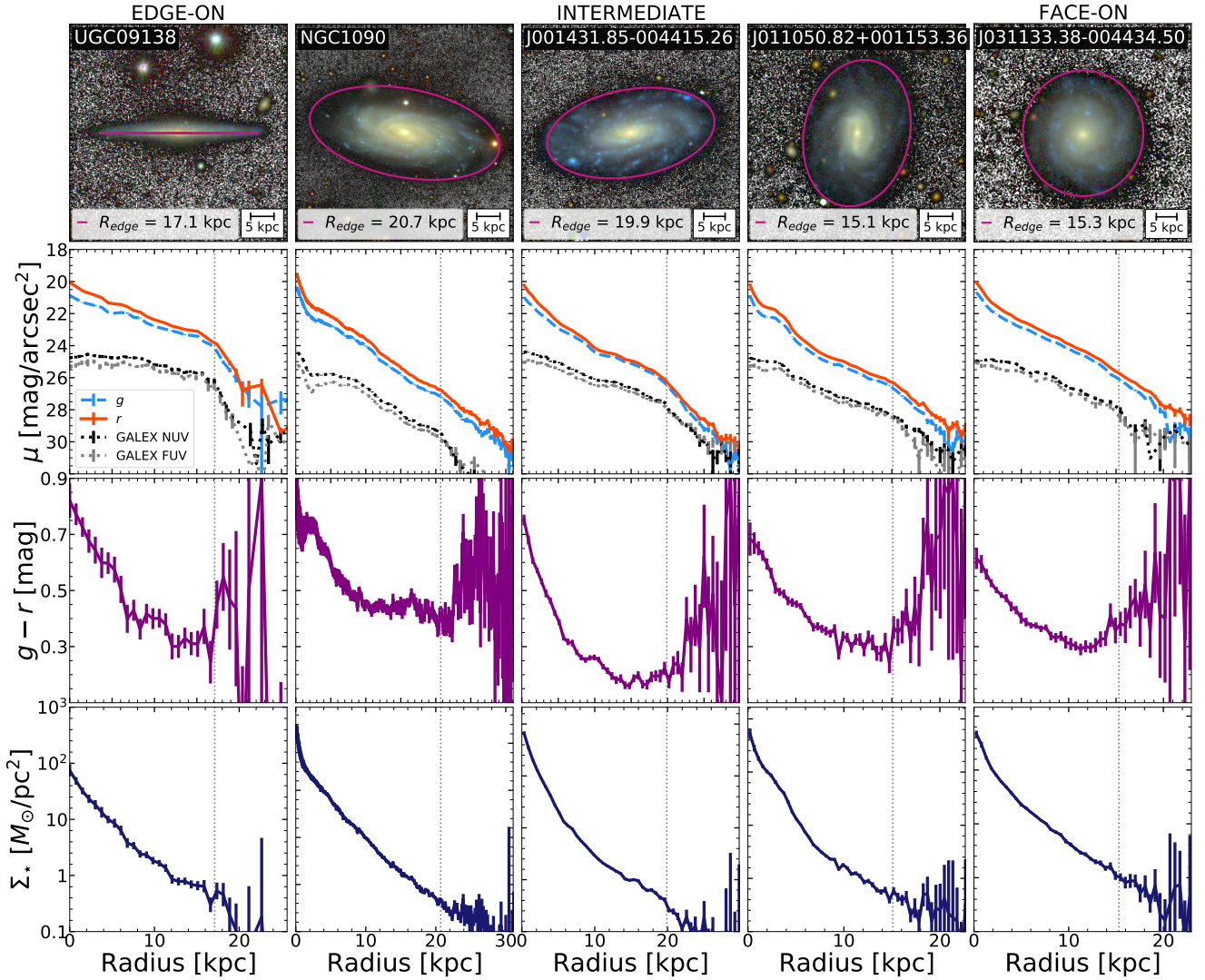


Fig. 2. Edges of galaxies as viewed in edge-on (*left*) to face-on (*right*) orientations. The galaxies were selected to have similar rotational velocities $V_{\text{rot}} \sim 145 \text{ km s}^{-1}$. *Left to right*: IAC Stripe 82 *gri*-colour composite image overlaid on a grey scaled *gri*-band summed image for contrast, surface brightness profiles in the SDSS *g*, *r*, GALEX NUV and FUV bands, *g* − *r* colour profile and the corresponding Σ_* stellar mass density profile. The pink contour in the *gri*-image and the vertical dotted lines in the other panels indicate the edge of the galaxy.

criteria to mark the edges of galaxies for future work using deeper and/or higher resolution data.

6. Results

Using the above procedure, we identified edges in 171 (or 61.2% of the) ellipticals, 273 (58.8% of) spirals and 180 (68.7% of) dwarfs (i.e 624 or 62% of the galaxies in total) in our parent sample and 21 galaxies in the collective **B12** and **P17** samples. The 381 galaxies with no identified edges in our parent sample comprise of 107 ellipticals, 190 spirals and 84 dwarfs. Eighty-seven galaxies within this sub-sample were removed due to heavy contamination from bright stars, neighbouring galaxies and clouds of Galactic cirrus. Such highly contaminated galaxies may be studied with ad-hoc techniques but this is beyond the scope of the analysis and pipelines we developed for this work. Further investigation reveals that the majority of galaxies without identified edges have very low inclination (mean axis-ratio of $q = 0.71$), 84% of which have $q > 0.5$. This finding is expected given the difficulty in identifying edges in low-inclination galaxies (see Fig. 2).

Figure 5 shows the main result of this work: the R_{edge} -stellar mass plane (left panels) and the $\Sigma_*(R_{\text{edge}})$ -stellar mass plane (right panels) for the parent sample. Each row shows the data points in both planes labelled according to each galaxy's morphology, colour and age at the edge. The latter relations are similar when the total magnitudes of the galaxy in *g* and *r* are used to compute the colour and age. Our results also do not change if we compute the age with a fixed metallicity $[M/H]$ of 0 or -0.71 (see Sect. 4). For clarity, we show our measurements for the nearby **B12** and **P17** galaxies separately in Fig. 6.

Following Trujillo et al. (2020) and Chamba et al. (2020), we obtain the best fit slopes and dispersion values for the scaling relations using a Huber Regressor (Huber 1964) which is a linear regression model robust to outliers. The global R_{edge} -stellar mass plane follows a power law of the form $R_{\text{edge}} \propto M_*^\beta$ where $\beta = 0.31 \pm 0.01$ and the relation has an observed dispersion of $\sigma_{R_{\text{edge}}} = 0.10 \pm 0.01$ dex. For the individual galaxy populations, β is 0.54 ± 0.03 for the elliptical galaxies (E0–S0+), 0.27 ± 0.02 for spirals (S0/a–Im) and 0.32 ± 0.03 for the dwarfs. If we remove the uncertainty from our visual identification of R_{edge} ($\sigma_{\text{vis}} \sim 0.04$ dex) which we computed using NC and IT's

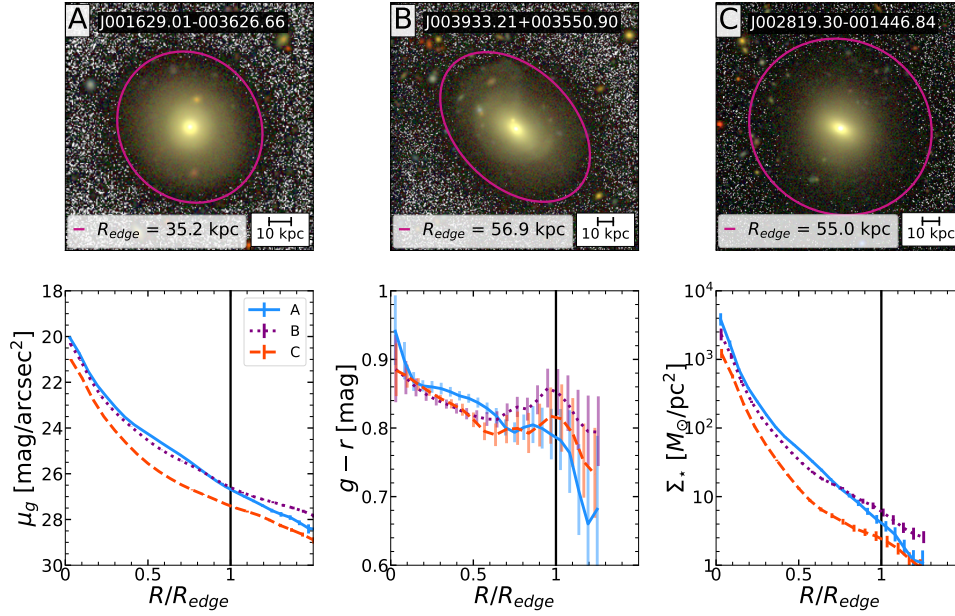


Fig. 3. Three examples of elliptical galaxies from the parent sample with stellar mass $\sim 10^{11} M_{\odot}$. *Top*: *gri*-band colour composite images, overlaid on the background *gri* summed image in grey scale, of the galaxies denoted as *A* (left), *B* (middle) and *C* (right). The SDSS J2000 identifier and R_{edge} are labelled for these galaxies as in Fig. 2. *Bottom, left to right*: the μ_g , $g-r$ and Σ_{\star} profiles of the objects. The edges for these galaxies are visible as a sudden transition from red to blue in their $g-r$ colour profiles (see Sect. 5.3 for details). The locations of the edges occur at mass densities $\Sigma_{\star}(R_{\text{edge}}) > 1 M_{\odot} \text{pc}^{-2}$.

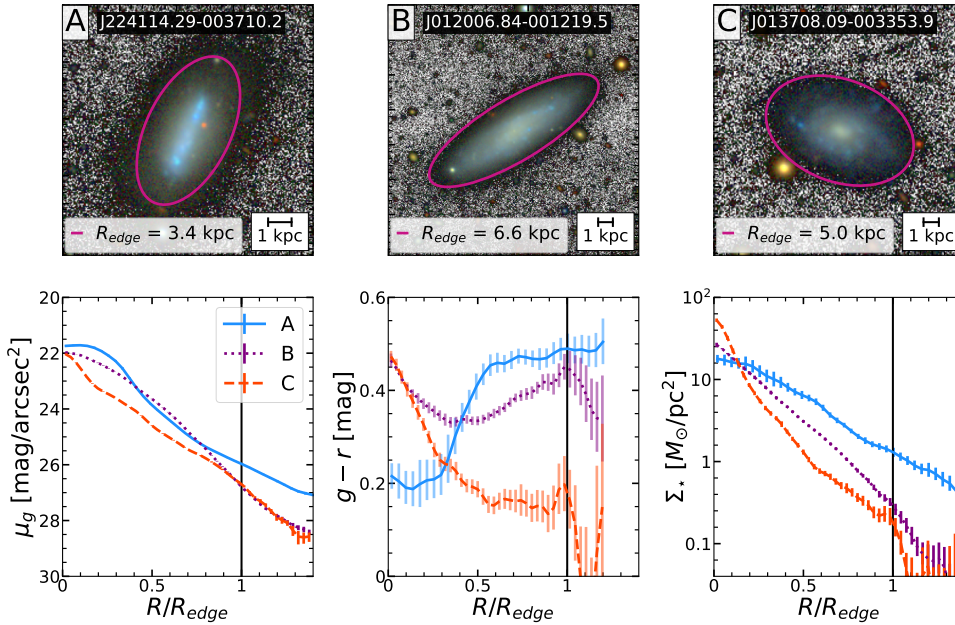


Fig. 4. Similar to Fig. 3, but for three dwarf galaxies with stellar mass $\sim 10^8 M_{\star}$. These examples were specifically chosen to illustrate the diversity in the colour profiles of this galaxy population and the criteria we use to locate the edge in these different cases. In case *A*, we use the change in slope in the Σ_{\star} profile. In *B* and *C*, the edge is identified as a sudden transition to bluer colours in the $g-r$ profile (see Sect. 5.4 for details). The edges of these galaxies occur at mass densities $\Sigma_{\star}(R_{\text{edge}}) \lesssim 2 M_{\odot} \text{pc}^{-2}$.

repeated measurements (see Sect 5.1) from $\sigma_{R_{\text{edge}}}$ in quadrature, we achieve a scatter of the relation $\bar{\sigma}_{R_{\text{edge}}} = 0.096 \pm 0.007$ dex. These values are provided in Table 1.

The above dispersion values also include observational errors due to background and stellar mass estimation. We find comparable values to the uncertainty in stellar mass in our galaxy sample to that published in Trujillo et al. (2020; i.e. 0.047 dex) and the effect of the background estimation on the location of R_{edge} amounts to 0.072 dex in our full sample. We may use these estimations of the uncertainty to compute the global intrinsic scatter of the size–stellar mass relation. Removing these values from $\sigma_{R_{\text{edge}}}$ in quadrature gives an intrinsic scatter of 0.059 dex. If we include the result of our visual identification of R_{edge} ($\sigma_{\text{vis}} \sim 0.04$ dex) the intrinsic scatter is 0.043 dex (but see Stone et al. 2021, for a detailed treatment of observational errors on the scatter of galaxy scaling relations).

In the case of the $\Sigma_{\star}(R_{\text{edge}})$ –stellar mass plane, we obtained two linear fits to describe the data by separating the sample in two intervals at $\log[M_{\star}/M_{\odot}] \sim 10.5$, in other words interval I_1

where $\log[M_{\star}/M_{\odot}] < 10.5$ and I_2 where $\log[M_{\star}/M_{\odot}] \geq 10.5$. We split our sample in this fashion because 1) a single polynomial fit to the data performed very poorly and 2) spiral galaxies are over represented in our sample (274 objects out of the 624 galaxies with identified edges). Therefore, by splitting the sample at a stellar mass of $\log[M_{\star}/M_{\odot}] \sim 10.5$, the two intervals I_1 and I_2 are more comparable in terms of sample size (294 and 330 galaxies, respectively) and it is also the location where the slope of the $\Sigma_{\star}(R_{\text{edge}})$ –stellar mass relation increases. We plot these results explicitly in Appendix D. The two linear fits may be used to determine the average location of the edge (in mass density) $\langle \Sigma_{\text{edge}}(M_{\star}) \rangle$, as a function of galaxy stellar mass, given by:

$$\log[\langle \Sigma_{\text{edge}}(M_{\star}) \rangle] = 0.13 \log \left[\frac{M_{\star}}{M_{\odot}} \right] - 1.32 \quad (\log \left[\frac{M_{\star}}{M_{\odot}} \right] < 10.5) \quad (3)$$

$$\log[\langle \Sigma_{\text{edge}}(M_{\star}) \rangle] = 0.39 \log \left[\frac{M_{\star}}{M_{\odot}} \right] - 3.97 \quad (\log \left[\frac{M_{\star}}{M_{\odot}} \right] \geq 10.5). \quad (4)$$

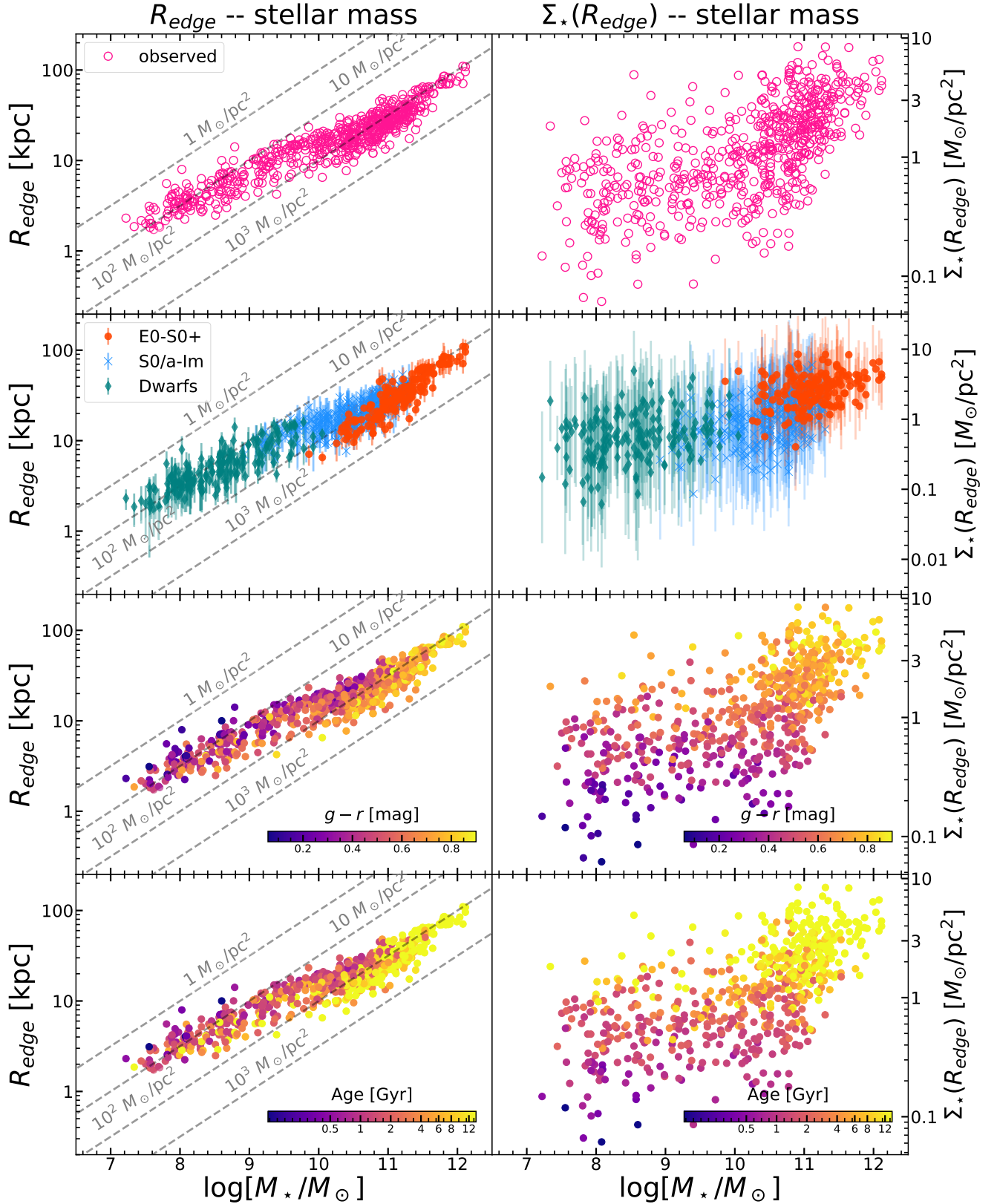


Fig. 5. R_{edge} –stellar mass (left) and $\Sigma_*(R_{\text{edge}})$ –stellar mass (right) relations derived in this work. Only those galaxies where an edge was identified are plotted (624 objects). The grey lines in the R_{edge} –stellar mass planes are lines of constant stellar mass surface density within the R_{edge} of the object. *Top to bottom:* each row shows the same observed relations (top), colour coded according to the morphology of the galaxies, $(g-r)_{\text{edge}}$ and a proxy for the age at R_{edge} , for a fixed metallicity $[M/H] = -0.71$. We plot the uncertainties in our measurements (see Sect. 4) only in the second row for clarity in the other panels.

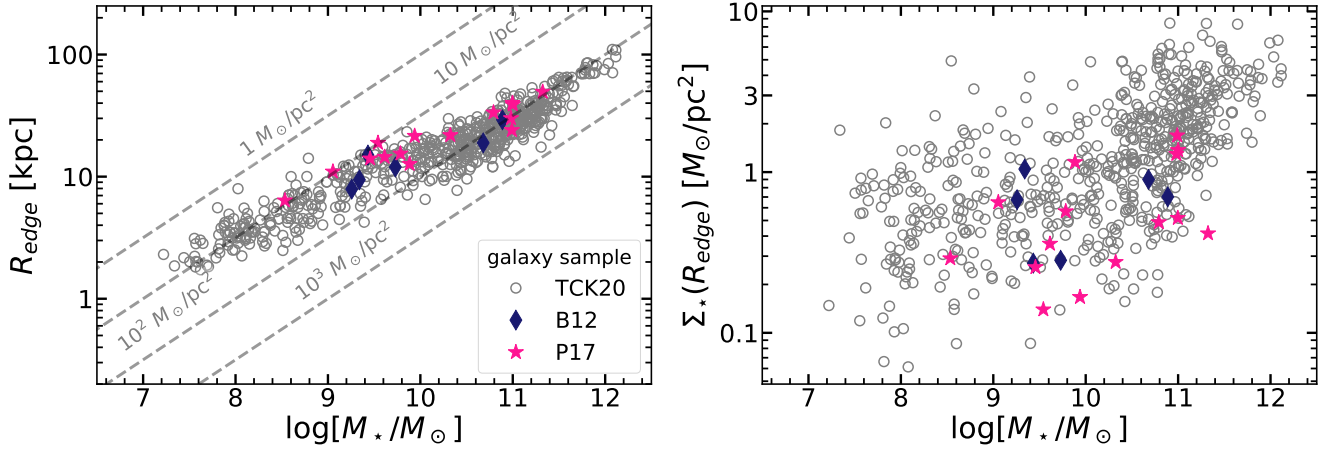


Fig. 6. Similar to Fig. 5, now including the measurements in this work for the sample of galaxies studied in B12 and P17. The grey circles are the measurements for our sample.

The uncertainties in the slopes $\beta_{I_1} = 0.13 \pm 0.03$ and $\beta_{I_2} = 0.39 \pm 0.06$ and the dispersion in both relations are similar: $\sigma_{I_1} = 0.29 \pm 0.02$ dex and $\sigma_{I_2} = 0.28 \pm 0.02$ dex.

We plot the distributions in R_{edge} and $\Sigma_{\star}(R_{\text{edge}})$ as histograms in Fig. 7 for each morphological group studied here (upper panels) and we use the linear fits to the R_{edge} – and $\Sigma_{\star}(R_{\text{edge}})$ –stellar mass planes to highlight the stratification in $(g-r)_{\text{edge}}$ colour in those relations (lower panels). The subscript ‘fit’ in this figure refers to the best fit line for each plane, which is the line that describes the average value of R_{edge} and $\Sigma_{\star}(R_{\text{edge}})$ at each stellar mass.

The main features of the results shown in the above figures are described in the following. Galaxies where $M_{\star} \lesssim 10^{11} M_{\odot}$ closely follow a power law of the form $R_{\text{edge}} \propto M_{\star}^{1/3}$ and is comparable to the global slope of the size–stellar mass relation. We additionally fit our data to a relation with a fixed slope of 1/3, restricting the sample only to spiral galaxies or to both spiral and dwarf galaxies, finding that the y-intercept using both sub-samples did not change. This result supports the idea that both populations lie on the same slope.

We also observe a tilt in the R_{edge} –stellar mass plane when $M_{\star} > 10^{11} M_{\odot}$. Massive elliptical galaxies dominate the scaling relation in this regime. At the same time, the mass density at the location of the edge depends on the total stellar mass of the galaxy with an up turn at $\log[M_{\star}/M_{\odot}] \sim 10.5$. The slope of the $\Sigma_{\star}(R_{\text{edge}})$ –stellar mass plane triples at this stellar mass.

In morphology, the average mass density at the location of the edge is $2.9 \pm 0.1 M_{\odot} \text{pc}^{-2}$ for the E0-S0+ sample, $1.1 \pm 0.04 M_{\odot} \text{pc}^{-2}$ for S0/a-Im and $0.6 \pm 0.03 M_{\odot} \text{pc}^{-2}$ for the dwarfs. In other words, the density is lower for dwarfs by almost a factor of five and two compared to the massive ellipticals and spirals, respectively.

The colour (age) gradient at fixed stellar mass with R_{edge} shows that larger galaxies have bluer (younger) edges. The observed colour gradient also produces a gradient in mass density at the location of the edge at fixed stellar mass where bluer edges are located in regions of lower mass densities. More specifically, for galaxies within a stellar mass range of 10^{10} – $10^{11} M_{\odot}$, we observe an age increase from ~ 2 Gyr to ~ 12 Gyr at the extreme ends of the scaling relation in R_{edge} as the size of the galaxy decreases, assuming a fixed metallicity of $[M/H] = -0.71$.

On average, galaxies located in the upper half of both the R_{edge} – and $\Sigma_{\star}(R_{\text{edge}})$ –stellar mass relations have bluer edges compared to the lower half. In Appendix B.2 we show that this

Table 1. Best-fit parameters for the R_{edge} –stellar mass relation.

Galaxy type	β	$\sigma_{R_{\text{obs}}}$	$\bar{\sigma}_{R_{\text{obs}}}$	r
R_{edge} –stellar mass				
All	0.31 ± 0.01	0.104 ± 0.010	0.096	0.95
E0-S0+	0.54 ± 0.03	0.094 ± 0.013	0.092	0.91
S0/a-Im	0.27 ± 0.02	0.097 ± 0.058	0.093	0.82
Dwarfs	0.32 ± 0.03	0.120 ± 0.012	0.118	0.85

Notes. β is the slope of the relation, $\sigma_{R_{\text{obs}}}$ is the dispersion, $\bar{\sigma}_{R_{\text{obs}}}$ is the observed dispersion corrected for visual identification errors (see text for details) and r is the Pearson correlation coefficient.

observation is not a bias due to image depth or the limiting surface brightness of our data.

The B12 and P17 galaxies lie in the upper half of the R_{edge} –stellar mass relation and in the lower regions of the $\Sigma_{\star}(R_{\text{edge}})$ –stellar mass relation. This is consistent with the fact that the majority of the galaxies in these samples have been classified with Sb, Sc or later morphology. We plot the R_{edge} – and $\Sigma_{\star}(R_{\text{edge}})$ –stellar mass relations only for the late-type galaxies in our sample in Fig. 8 to highlight this statement.

7. Discussion

We have visually identified the edges of a large sample of ~ 1000 low-inclination galaxies spanning a wide morphology (from dwarfs to ellipticals) and stellar mass range ($10^7 M_{\odot} < M_{\star} < 10^{12} M_{\odot}$). Sixty-two percent of the galaxies in our total sample presented identifiable edges following our visualisation procedure. We estimated the stellar mass density at their edge and then presented the resulting R_{edge} – and $\Sigma_{\star}(R_{\text{edge}})$ –stellar mass relations for these galaxies.

Our main results are discussed in the following sub-sections. We leave the exploration of how our work may be used in future large-scale catalogues in Appendix E. We find that the $\Sigma_{\star}(R_{\text{edge}})$ –stellar mass relations in Eqs. (3) and (4) could be used to obtain the location of the edge and provide a proxy for the size of any galaxy, provided its stellar mass is known. These laws may be useful for larger galaxy samples and automated cataloguing in future multi-band surveys such as Rubin Observatory’s Legacy Survey of Space and Time (LSST).

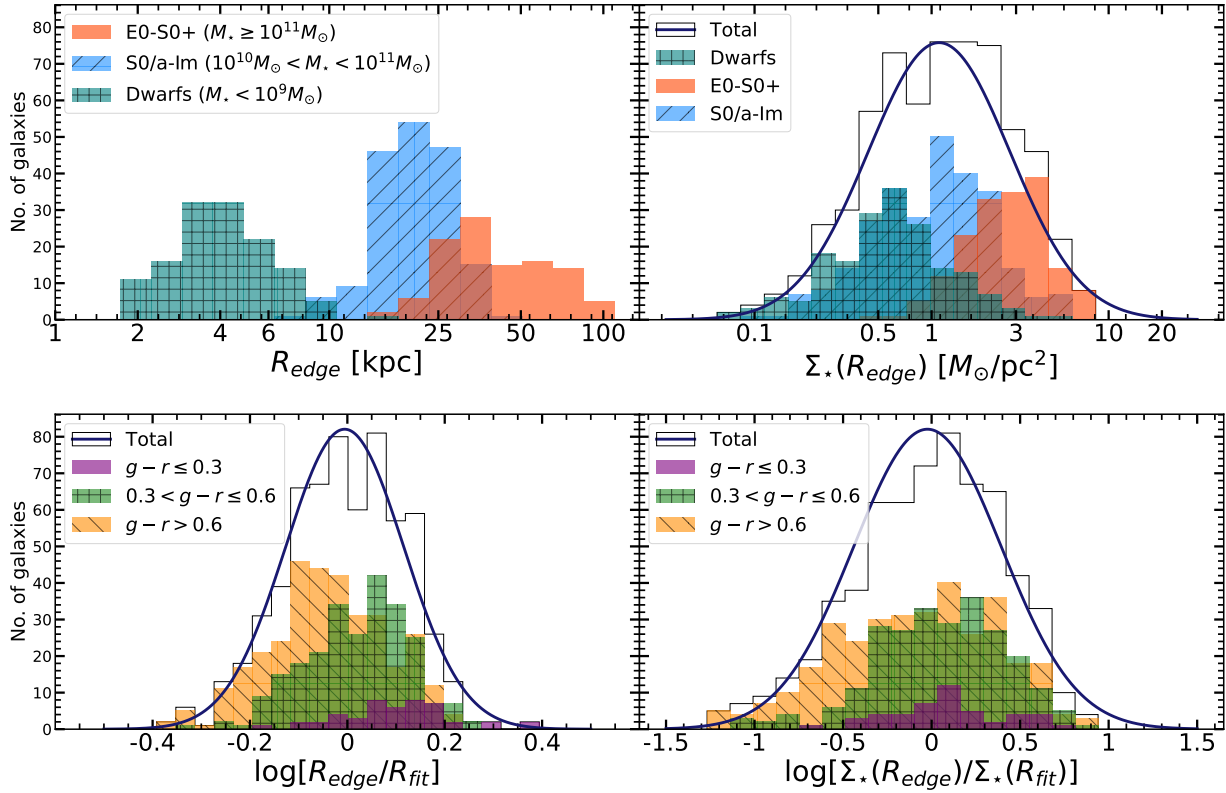


Fig. 7. Representation of the results shown in Fig. 5 as histograms. *Top:* the distribution of R_{edge} (left) and $\Sigma_*(R_{\text{edge}})$. *Bottom:* the distribution of $(g-r)_{\text{edge}}$ in the R_{edge} –stellar mass (left) and $\Sigma_*(R_{\text{edge}})$ –stellar mass (right) relations. The subscript ‘fit’ refers to the best fit line of each plane.

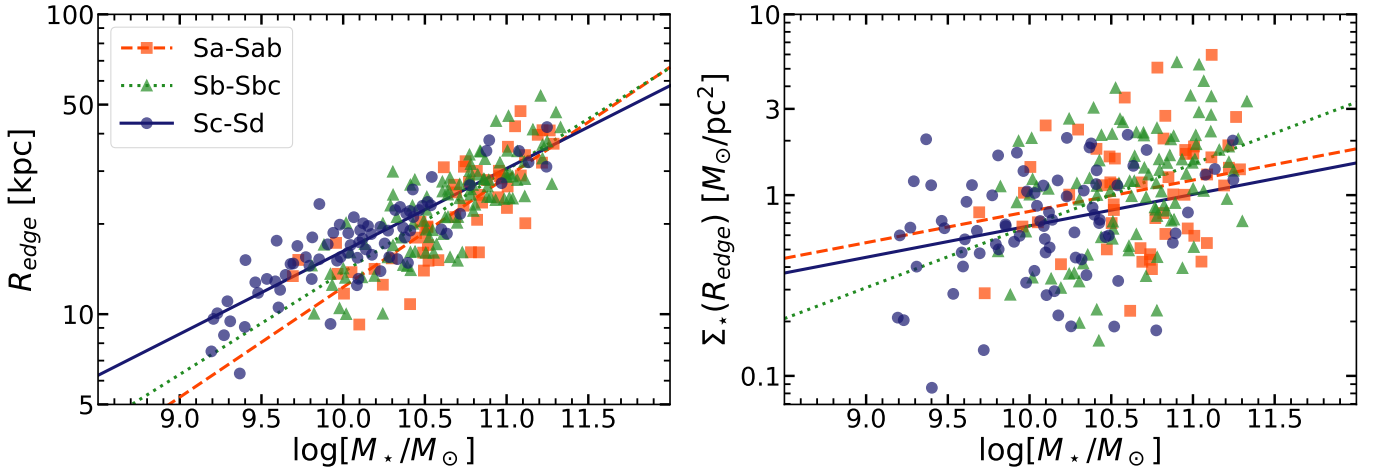


Fig. 8. Stratification of late-type galaxies in the R_{edge} –stellar mass (left) and $\Sigma_*(R_{\text{edge}})$ –stellar mass (right) relation. The galaxies are grouped morphologically following Trujillo et al. (2020). The lines are the best-fit relations for each group in both panels. See text for details.

7.1. The global slope of size–stellar mass relation:

$$R_{\text{edge}} \propto M_*^{1/3}$$

If we focus on the spirals and dwarfs in our study, we have found that these galaxy populations have R_{edge} –stellar mass relations with comparable slopes ($\beta \sim 0.3$ and close to a global slope $\sim 1/3$; see Table 1), with an intrinsic dispersion $\lesssim 0.06$ dex. These parameters are compatible with those obtained in Trujillo et al. (2020) using R_1 (the fixed isomass contour at $1 M_\odot \text{ pc}^{-2}$) for size. The global slope of $1/3$ is observed over four orders of magnitudes in stellar mass $10^7 M_\odot < M_* < 10^{11} M_\odot$ in the size–stellar mass relation, despite the different stellar mass surface densities we measured at the edges of galaxies in this regime. The lower

density we measure at the edge for dwarfs ($\sim 0.6 M_\odot \text{ pc}^{-2}$) compared to the spirals ($\sim 1 M_\odot \text{ pc}^{-2}$) could be reflective of the low star formation efficiency that has been observed in these galaxies (e.g., Leroy et al. 2008; Huang et al. 2012). However, despite this difference, the constant slope could imply that the dwarfs and spiral galaxies in our sample share a common mechanism by which in situ star formation may have occurred. This idea is not incompatible with the fact that several similarities in the structure of surface brightness, colour and stellar mass density profiles of dwarfs and spiral galaxies have been found in the literature within the context of galaxy outskirts (e.g., Hunter et al. 2011; Herrmann et al. 2016).

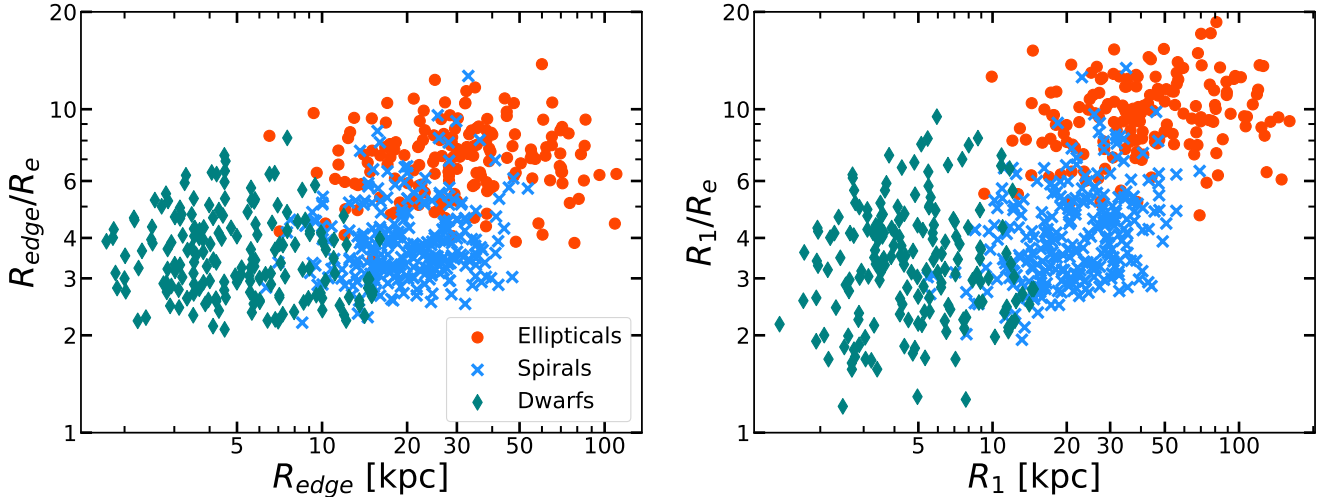


Fig. 9. Ratios R_{edge}/R_e (left) and R_1/R_e (right) as a function of the respective sizes for the labelled morphologies. The diagrams reinforce how extended galaxies are compared to what the effective radius represents R_e .

We contrast this result with those obtained using the effective radius (R_e ; de Vaucouleurs 1948), a popular measure for galaxy size in the literature and with which the resulting size–stellar mass plane has very different characteristics. The relation is more broken for different galaxy morphologies (see e.g., Shen et al. 2003; Brodie et al. 2011) and the dispersion is almost three times larger than that of the R_{edge} –stellar mass plane (see also Trujillo et al. 2020). The broken scaling relations shown in these previous studies using R_e have traditionally been interpreted to reflect different size formation or evolution mechanisms for the galaxies. From this perspective, the global slope representing an unbroken size–stellar mass relation found here does not obviously favour such interpretations and works to readdress these issues are currently ongoing. However, to give the reader a view on how extended the galaxies in our sample are compared to what R_e suggests, we plot the ratios R_{edge}/R_e and R_1/R_e as a function of the respective sizes in Fig. 9. We compute R_e in a model independent way using the growth curve of the galaxy in the g -band which is our deepest dataset. The R_1 values were taken from Trujillo et al. (2020).

Particularly in R_{edge} , it is clear for each galaxy type that while there is a change in R_{edge} over tens of kiloparsecs (for example from 10 to 50 kpc for spirals), the ratio with R_e is small (about 3–4). These results further support the need to rethink the concept of galaxy size and readdress the origin of the size–stellar mass relation (Chamba 2020).

7.2. Comparison between R_{edge} and the isomass contour at $1 M_{\odot} \text{pc}^{-2}$

To further address the structure we have observed in the size–stellar mass relation (stratification and slopes), it is worth exploring how similar R_{edge} is compared to R_1 . As mentioned in the Introduction, we studied the R_1 –stellar mass relation in Trujillo et al. (2020) and Chamba et al. (2020) because the isomass contour at $1 M_{\odot} \text{pc}^{-2}$ is physically motivated for Milky-Way-like galaxies as it is related to a star formation threshold. A fixed isomass contour at $1 M_{\odot} \text{pc}^{-2}$ is also easier to measure⁷ and reproduce which makes it more robust. For the sam-

ple of galaxies analysed here, we find that R_1 appears at a similar surface brightness to R_{edge} : on average R_1 appears at $\mu_g = 27.4 \pm 0.05 \text{ mag arcsec}^{-2}$ in g (the standard deviation of this distribution is 1.2 mag) and R_{edge} can be $0.4 \pm 0.02 \text{ mag arcsec}^{-2}$ brighter on average. Figure 10 shows R_{edge} vs. R_1 , colour coded according to the galaxy’s stellar mass (top) and morphology (middle). The lower panel shows the histogram of the distribution in the R_{edge} – R_1 plane, with the sample divided according to their labelled morphology. The scatter in the R_{edge} vs. R_1 distribution is 0.088 dex with the elliptical (dwarf) galaxy population having smaller (slightly larger) R_{edge} than R_1 by ~ 0.1 dex (0.05 dex) on average. Given these results, we recommend the use of R_1 for galaxies of similar properties as those studied here if the measurement of R_{edge} is not possible due to, for instance, poor signal-to-noise ratios.

This result allows us to explore the R_1 of galaxies where we did not identify the presence of an edge. In Fig. 11 we plot the R_1 of these galaxies (381 galaxies; 37% of the total sample) on the R_{edge} –stellar mass plane. The majority of these galaxies have very low inclinations or are heavily contaminated in their outskirts (see Sect. 6). We see that the R_1 of these galaxies follow the overall distribution of R_{edge} in the size–mass plane within the uncertainties of our R_{edge} measurements. The most visible deviation occurs at the higher mass end ($M_{\star} > 10^{11} M_{\odot}$), however, this can be explained by the fact that the majority of our elliptical galaxies have R_{edge} at surface densities $> 1 M_{\odot} \text{pc}^{-2}$ and thus results in smaller sizes (below the black points). In contrast, the R_1 of all of the dwarf galaxies shown here appear to be within the distribution of R_{edge} , even though R_{edge} of the dwarfs are on average slightly larger (lower panel of Fig. 10). Therefore, from Fig. 11 we may conclude that the exclusion of these galaxies without identified edges from our work does not bias our analysis and the main results discussed in this section remain unchanged. However, we note that the scatter using R_1 is smaller compared to R_{edge} because of the difficulty in measuring the edge compared to a fixed isomass contour.

7.3. The tilt in the R_{edge} – and $\Sigma_{\star}(R_{\text{edge}})$ –stellar mass planes

The comparison between R_{edge} and R_1 above shows that the two measures deviate from the one-to-one relation (solid black line in Fig. 10) for the majority of the higher mass elliptical

⁷ R_1 can be measured provided that the data is sufficiently deep, for example deeper than SDSS for low-inclination galaxies; see Fig. 6 in Trujillo et al. (2021).

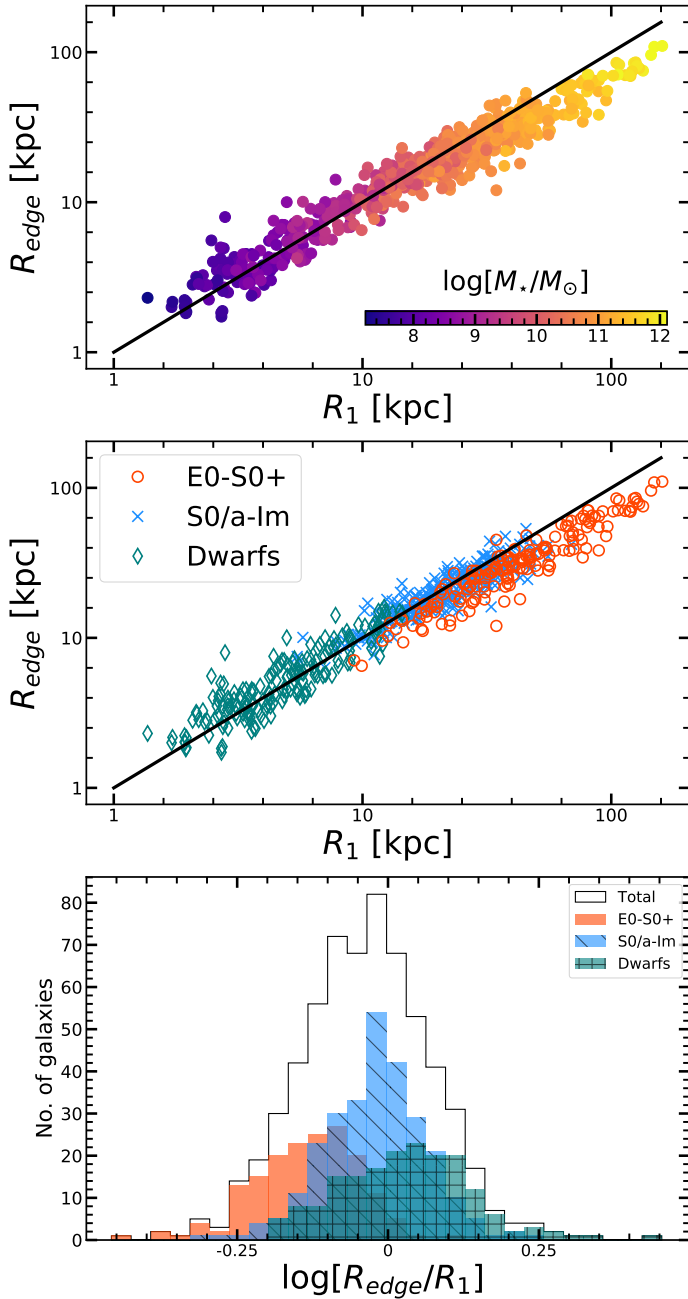


Fig. 10. Comparison between R_{edge} and R_1 . The *top and middle panels* show R_{edge} vs. R_1 for the galaxies in our sample, colour coded in stellar mass and morphology, respectively. The solid black line in the upper panels is the one-to-one relation. The *lower panel* shows the same distribution as a histogram.

galaxies in our sample (especially when $M_\star > 10^{11} M_\odot$), with $R_{\text{edge}} < R_1$. Consequently, R_{edge} appears at stellar mass densities $> 1 M_\odot \text{pc}^{-2}$ ($\sim 3 M_\odot \text{pc}^{-2}$ on average) for these galaxies and can be seen as a tilt in the R_{edge} - and $\Sigma_\star(R_{\text{edge}})$ -stellar mass relations (Fig. 5). A similar tilt was observed in the R_1 -stellar mass plane in Trujillo et al. (2020), however, here we have additionally found that the edges of these galaxies have older stellar populations than the late-types ($g-r$ colour > 0.6). The tilt observed here (characterised by the slope of the size-stellar mass plane) is two times steeper for the ellipticals than the spirals and could be additional evidence towards a major difference in the mechanisms responsible for size growth between these two morpho-

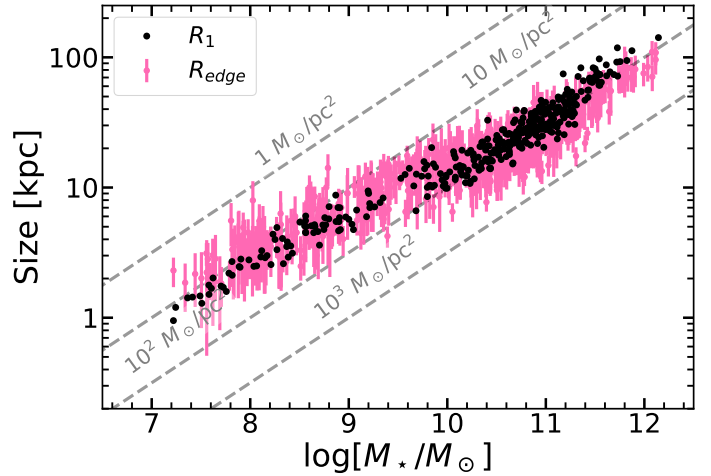


Fig. 11. R_1 of galaxies where we were unable to locate the presence of edges (black) over plotted on the R_{edge} -stellar mass plane (pink).

logical groups, such as accretion which predominantly occurs in the most massive galaxies.

To understand why the star formation threshold for elliptical galaxies is higher than for spiral galaxies, we need to consider the epoch at which these massive galaxies initially formed their stars. As pointed out in Trujillo et al. (2020), it has been observed that massive elliptical galaxies had bursty star formation histories at high redshift with star formation rates as extreme as $1000 M_\odot \text{yr}^{-1}$ (e.g., Riechers et al. 2013; Jaskot et al. 2015). A high rate of star formation could provide a large enough energy budget to the surrounding gas, making it difficult for stars to form preferentially at low surface densities by increasing the galaxy's star formation threshold. Therefore, the edges of these massive galaxies could be tracing star formation that occurred during an epoch of high star formation rate which formed the core (bulge) material of the galaxy. Notice that $M_\star > 10^{11} M_\odot$ is also the regime where pressure supported systems could be dominating the scaling relation compared to rotationally supported galaxies (see Emsellem et al. 2011). This difference (as well as in symmetry, considering spherical vs. disk) between these galaxies could have consequences on the density at which stars would have preferentially formed in galaxies in the early Universe.

We have selected a specific criterion to locate the edges of elliptical galaxies: a sudden colour transition from red to blue (Sect. 5.3) and we have left the exploration of alternative criteria for future work. However, based on our results it is interesting to consider that deviations from the global slope in the size-stellar mass relation $R_{\text{edge}} \sim M_\star^{1/3}$ could indicate deviations from the early star formation phase in the core component of these galaxies. If we fix the most massive galaxies with $M_\star > 10^{11.5} M_\odot$ (i.e. where only elliptical galaxies in our sample deviate from the global slope) to lie on the $R_{\text{edge}} \sim M_\star^{1/3}$ relation, we obtain that their R_{edge} would be on average almost ~ 20 kpc smaller. Consequently, the stellar mass density at these locations is more than double compared to that of the identified edges for these galaxies (i.e. $\sim 8 M_\odot \text{pc}^{-2}$ on average). Such a threshold would enclose the bulk of the stellar component in relic galaxies, which are those galaxies that represent the core component of the majority of elliptical galaxies in the nearby Universe (e.g., NGC 1277; Trujillo et al. 2014). This alternative criterion would also better represent the visual edge of case C shown in Fig. 3. With either this new criterion or that adopted in our identification procedure (Sect. 5.1), if the edges indicate a star formation threshold, our

conclusion that the edges of elliptical galaxies occur at higher stellar mass densities remains unchanged.

7.4. The stratification of late-types

A stratification of late-type galaxies in morphology was previously found by [Saintonge & Spekkens \(2011\)](#) and [Trujillo et al. \(2020\)](#) using $R_{23.5}$ (the isophote at 23.5 mag arcsec⁻² in the SDSS *i*-band) and R_1 respectively, with its origin still unknown. However, with R_{edge} we have found that while the average stellar mass density at the star formation threshold for these galaxies is $1 M_{\odot} \text{pc}^{-2}$, there appears to be an additional variation in their stellar population properties where larger galaxies have bluer edges (Figs. 5, 6 and 8).

The stratification in size and colour suggests that larger galaxies may have reached their current size at a later time than smaller ones. This interpretation follows from the assumption that bluer colours trace ongoing or recent star formation while redder colours reflect the presence of older stellar material. For galaxies within the 10^{10} – $10^{11} M_{\odot}$ stellar mass range studied here, outskirts that are populated with young to intermediate aged stars (<6 Gyr) are possible due to, for example, the accretion of gas-rich satellite galaxies that trigger new star formation (e.g., [Grand et al. 2017](#)), the galaxy’s enriched HI content (e.g., [Kauffmann 2015](#)) or the migration of stars from the disk to the outskirts (e.g., [Roškar et al. 2008](#)). Of course the latter scenario could also result in redder outskirts with older stars but star formation may still occur in these regions (see the review by [Elmegreen & Hunter 2017](#)).

The idea that larger late-type galaxies are generally younger⁸ is also not incompatible with the stratification we observe in their global morphology with Sa-Sab galaxies showing smaller sizes compared to Sc-Sd types (see Fig. 8). Sa-Sab galaxies generally have lower star formation rates (often in a path towards quenching) than Sc or other later types where they are much higher (e.g., [González Delgado et al. 2016](#); [Bait et al. 2017](#)). Our data could be reflective of this difference between galaxy types. Additionally, the lower half of the size–stellar mass relation is populated by elliptical galaxies of similar stellar mass (see Fig. 5). Elliptical galaxies are generally red, old and quiescent. From this perspective, the stratification we observe could be connected to when galaxies reached their present day stellar mass. In other words, a stratification between the ‘newer’ late-type spirals and the ‘older’ early-type elliptical galaxies (see also the recent work by [Watkins et al. 2022](#)).

The interpretation of whether a stratification in morphology exists in the lower mass dwarf regime is likely subjected to incompleteness effects (due to the limit in magnitude selected for spectroscopic targets in SDSS; see the discussion in [Chamba et al. 2020](#)). However, at least from the lower panels of Fig. 7, there appears to be a stratification of galaxy size in colour where all of the blue edged dwarf galaxies ($g - r \lesssim 0.3$) appear in the upper half of the size–stellar mass relation. We do not possess morphological information of these galaxies in our sample to investigate this here further and leave it for future work.

8. Conclusions

We have identified the edges of one of the largest samples of low-inclination galaxies. Our work expands on a physically motivated approach to define the edges (and consequently the sizes)

of galaxies as the outermost location where in situ star formation (either ongoing or in the past) significantly drops within these systems. This idea is based on the gas density threshold required for the star formation process in galaxies (e.g., [Schaye 2004](#)). Our main conclusions can be summarised as follows:

- The size–stellar mass relation using R_{edge} has a global slope of $\sim 1/3$ and an intrinsic scatter $\lesssim 0.06$ dex over a wide stellar mass range $10^7 M_{\odot} < M_{\star} < 10^{12} M_{\odot}$ suggesting a common mechanism of in situ star formation. The structure of the relation is similar to that using R_1 (see [Trujillo et al. 2020](#); [Chamba et al. 2020](#)).
- Massive elliptical galaxies dominate the scaling relation when $M_{\star} \gtrsim 10^{11} M_{\odot}$. This region corresponds to the tilt in the R_{edge} – and $\Sigma_{\star}(R_{\text{edge}})$ –stellar mass planes where the slope of the size–stellar mass relation doubles, potentially tracing the different epoch and high efficiency at which massive galaxies formed their stars.
- The stellar mass surface density at the edge (and consequently the star formation threshold) is a function of stellar mass and depends on the morphology of galaxies: it averages to $\sim 3 M_{\odot} \text{pc}^{-2}$ (or higher) for ellipticals, $\sim 1 M_{\odot} \text{pc}^{-2}$ for spirals and $\sim 0.6 M_{\odot} \text{pc}^{-2}$ for dwarfs.
- R_{edge} is larger for bluer (i.e. younger) galaxies at a fixed stellar mass, reflective of when these galaxies reached their present-day size.

Given that R_{edge} is very similar to the location of the $1 M_{\odot} \text{pc}^{-2}$ isomass contour (R_1) for the majority of the galaxies, we recommend the use of the latter (or a higher isomass contour for elliptical galaxies) when the measurement of R_{edge} is challenging, for example due to imaging with low signal-to-noise. Due to the low scatter and physical significance underlying our measurements, we propose our size definition to be used in future deep, large-scale catalogues such as those from the LSST, to reach extreme galaxies of low surface brightness or high redshift galaxies with JWST and shift our understanding of how galaxies truly grow in size.

Acknowledgements. We thank the anonymous referee for their detailed comments which helped to significantly improve the clarity of this manuscript. We acknowledge financial support from the State Research Agency (AEI-MCINN) of the Spanish Ministry of Science and Innovation under the grant ‘The structure and evolution of galaxies and their central regions’ with reference PID2019-105602GB-I00/10.13039/501100011033 and grant PID2019-107427GB-C32, and from IAC projects P/300624 and P/300724, financed by the Ministry of Science and Innovation, through the State Budget and by the Canary Islands Department of Economy, Knowledge and Employment, through the Regional Budget of the Autonomous Community. N.C. acknowledges support from the research project grant ‘Understanding the Dynamic Universe’ funded by the Knut and Alice Wallenberg Foundation under Dnr KAW 2018.0067 and thanks Matthew Hayes, Fernando Buitrago, Claudio Dalla Vecchia, Aura Obreja, L. Pascho, and Naomi Samsodeen for interesting discussions. J.H.K. and I.T.C. acknowledge support from the ACIISI, Consejería de Economía, Conocimiento y Empleo del Gobierno de Canarias and the European Regional Development Fund (ERDF) under grant with reference PROID2021010044. Funding for the Sloan Digital Sky Survey IV has been provided by the Alfred P. Sloan Foundation, the U.S. Department of Energy Office of Science, and the Participating Institutions. SDSS-IV acknowledges support and resources from the Center for High-Performance Computing at the University of Utah. The SDSS web site is www.sdss.org. SDSS-IV is managed by the Astrophysical Research Consortium for the Participating Institutions of the SDSS Collaboration including the Brazilian Participation Group, the Carnegie Institution for Science, Carnegie Mellon University, the Chilean Participation Group, the French Participation Group, Harvard-Smithsonian Center for Astrophysics, Instituto de Astrofísica de Canarias, The Johns Hopkins University, Kavli Institute for the Physics and Mathematics of the Universe (IPMU)/University of Tokyo, the Korean Participation Group, Lawrence Berkeley National Laboratory, Leibniz Institut für Astrophysik Potsdam (AIP), Max-Planck-Institut für Astronomie (MPIA Heidelberg), Max-Planck-Institut für Astrophysik (MPA Garching), Max-Planck-Institut für Extraterrestrische Physik (MPE), National Astronomical Observatories of China, New Mexico State University, New York

⁸ The stratification in colour does not change whether we use the global $g - r$ of the galaxy or the colour at the edge.

University, University of Notre Dame, Observatório Nacional/MCTI, The Ohio State University, Pennsylvania State University, Shanghai Astronomical Observatory, United Kingdom Participation Group, Universidad Nacional Autónoma de México, University of Arizona, University of Colorado Boulder, University of Oxford, University of Portsmouth, University of Utah, University of Virginia, University of Washington, University of Wisconsin, Vanderbilt University, and Yale University. This research has made use of the NASA/IPAC Extragalactic Database (NED), which is operated by the Jet Propulsion Laboratory, California Institute of Technology, under contract with the National Aeronautics and Space Administration. We acknowledge the usage of the HyperLeda database <http://leda.univ-lyon1.fr>. This work was partly done using GNU Astronomy Utilities (Gnuastro, <http://www.gnuastro.org>) version 0.14. Work on Gnuastro has been funded by the Japanese Ministry of Education, Culture, Sports, Science, and Technology (MEXT) scholarship and its Grant-in-Aid for Scientific Research (21244012, 24253003), the European Research Council (ERC) advanced grant 339659-MUSICOS, European Union's Horizon 2020 research and innovation programme under Marie Skłodowska-Curie grant agreement No 721463 to the SUNDIAL ITN, and from the Spanish Ministry of Economy and Competitiveness (MINECO) under grant number AYA2016-76219-P. *Software:* Astropy, (<http://www.astropy.org>) a community-developed core Python package for Astronomy (Robitaille et al. 2013; Price-Whelan et al. 2018); Gnuastro (astwarp; Akhlaghi & Ichikawa 2015); IMFIT (Erwin 2015); Jupyter Notebooks (Kluyver et al. 2016); Matplotlib (Hunter 2007); MTOBJects (Teeninga et al. 2016; Haigh et al. 2021); NumPy (Oliphant 2006; Walt 2011); SAO Image DS9 (Smithsonian Astrophysical Observatory 2000); SciPy (Jones et al. 2001); SWarp (Bertin 2010); and TOPCAT (Taylor 2005).

References

- Abazajian, K. N., Adelman-McCarthy, J. K., Agüeros, M. A., et al. 2009, *ApJS*, **182**, 543
- Akhlaghi, M., & Ichikawa, T. 2015, *ApJS*, **220**, 1
- Azzollini, R., Trujillo, I., & Beckman, J. E. 2008, *ApJ*, **679**, L69
- Bait, O., Barway, S., & Wadadekar, Y. 2017, *MNRAS*, **471**, 2687
- Bakos, J., & Trujillo, I. 2012, ArXiv e-prints [arXiv:1204.3082]
- Bakos, J., Trujillo, I., & Pohlen, M. 2008, *ApJ*, **683**, L103
- Bertin, E. 2010, *SWarp: Resampling and Co-adding FITS Images Together* (Astrophysics Source Code Library)
- Brodie, J. P., Romanowsky, A. J., Strader, J., & Forbes, D. A. 2011, *AJ*, **142**, 199
- Cardona-Barrero, S., Di Cintio, A., Battaglia, G., Macciò, A. V., & Taibi, S. 2022, ArXiv e-prints [arXiv:2206.10481]
- Chamba, N. 2020, *Res. Notes Am. Astron. Soc.*, **4**, 117
- Chamba, N., Trujillo, I., & Knapen, J. H. 2020, *A&A*, **633**, L3
- Crnojević, D. 2017, in *Outskirts of Galaxies*, eds. J. H. Knapen, J. C. Lee, & A. Gil de Paz, *Astrophys. Space Sci. Lib.*, **434**, 31
- de Vaucouleurs, G. 1948, *Annales d'Astrophysique*, **11**, 247
- Díaz-García, S., Comerón, S., Courteau, S., et al. 2022, *A&A*, in press, <https://doi.org/10.1051/0004-6361/202142447>
- Efstathiou, G., & Silk, J. 1983, *Fund Cosmic. Phys.*, **9**, 1
- Elmegreen, B. G., & Hunter, D. A. 2017, *Astrophys. Space Sci. Lib.*, **434**, 115
- Emsellem, E., Cappellari, M., Krajnović, D., et al. 2011, *MNRAS*, **414**, 888
- Erwin, P. 2015, *ApJ*, **799**, 226
- Fall, S. M., & Efstathiou, G. 1980, *MNRAS*, **193**, 189
- Fliri, J., & Trujillo, I. 2016, *MNRAS*, **456**, 1359
- Font, A. S., McCarthy, I. G., Poole-Mckenzie, R., et al. 2020, *MNRAS*, **498**, 1765
- Gaia Collaboration (Brown, A. G. A., et al.) 2016, *A&A*, **595**, A2
- González Delgado, R. M., Cid Fernandes, R., Pérez, E., et al. 2016, *A&A*, **590**, A44
- Grand, R. J. J., Gómez, F. A., Marinacci, F., et al. 2017, *MNRAS*, **467**, 179
- Haigh, C., Chamba, N., Venhola, A., et al. 2021, *A&A*, **645**, A107
- Herrmann, K. A., Hunter, D. A., & Elmegreen, B. G. 2016, *AJ*, **151**, 145
- Holmberg, E. 1958, *Meddelanden fran Lunds Astronomiska Observatorium Serie II*, **136**, 1
- Huang, S., Haynes, M. P., Giovanelli, R., & Brinchmann, J. 2012, *ApJ*, **756**, 113
- Huang, S., Leauthaud, A., Bradshaw, C., et al. 2022, *MNRAS*, **515**, 4722
- Huber, P. J. 1964, *Ann. Math. Stat.*, **35**, 73
- Hunter, J. D. 2007, *Comput. Sci. Eng.*, **9**, 90
- Hunter, D. A., Elmegreen, B. G., Oh, S.-H., et al. 2011, *AJ*, **142**, 121
- Infante-Sainz, R., Trujillo, I., & Román, J. 2020, *MNRAS*, **491**, 5317
- Jaskot, A. E., Oey, M. S., Salzer, J. J., et al. 2015, *ApJ*, **808**, 66
- Jiang, L., Fan, X., Annis, J., et al. 2008, *AJ*, **135**, 1057
- Jing, J., Liu, S., Wang, G., Zhang, W., & Sun, C. 2022, *Neurocomputing*, **503**, 259
- Jones, E., Oliphant, T., Peterson, P., et al. 2001, SciPy: Open source scientific tools for Python, <http://www.scipy.org/>
- Kauffmann, G. 2015, *MNRAS*, **450**, 618
- Kennicutt, R. C., Jr 1989, *ApJ*, **344**, 685
- Kluyver, T., Ragan-Kelley, B., Pérez, F., et al. 2016, in *Positioning and Power in Academic Publishing: Players, Agents and Agendas*, eds. F. Loizides, & B. Schmidt, (IOS Press), 87
- Kniazev, A. Y., Grebel, E. K., Pustilnik, S. A., et al. 2004, *AJ*, **127**, 704
- Leroy, A. K., Walter, F., Brinks, E., et al. 2008, *AJ*, **136**, 2782
- Makarov, D., Prugniel, P., Terekhova, N., Courtois, H., & Vauglin, I. 2014, *A&A*, **570**, A13
- Maraston, C., Pforr, J., Henriques, B. M., et al. 2013, *MNRAS*, **435**, 2764
- Martin, D. C., Fanson, J., Schiminovich, D., et al. 2005, *ApJ*, **619**, L1
- Martín-Navarro, I., Trujillo, I., Knapen, J. H., Bakos, J., & Fliri, J. 2014, *MNRAS*, **441**, 2809
- Martínez-Lombilla, C., Trujillo, I., & Knapen, J. H. 2019, *MNRAS*, **483**, 664
- Monelli, M., & Trujillo, I. 2019, *ApJ*, **880**, L11
- Morrissey, P., Conrow, T., Barlow, T. A., et al. 2007, *ApJS*, **173**, 682
- Nair, P. B., & Abraham, R. G. 2010, *ApJS*, **186**, 427
- Neumann, J., Thomas, D., Maraston, C., et al. 2021, *MNRAS*, **508**, 4844
- Oliphant, T. 2006, *NumPy: A guide to NumPy* (USA: Trelgol Publishing)
- Peters, S. P. C., van der Kruit, P. C., Knapen, J. H., et al. 2017, *MNRAS*, **470**, 427
- Price-Whelan, A., Sipőcz, B., Günther, H., et al. 2018, *AJ*, **156**, 123
- Quirk, W. J. 1972, *ApJ*, **176**, L9
- Radburn-Smith, D. J., de Jong, R. S., Streich, D., et al. 2014, *ApJ*, **780**, 105
- Riechers, D. A., Bradford, C. M., Clements, D. L., et al. 2013, *Nature*, **496**, 329
- Robitaille, T. P., Tollerud, E. J., Greenfield, P., et al. 2013, *A&A*, **558**, A33
- Roediger, J. C., & Courteau, S. 2015, *MNRAS*, **452**, 3209
- Román, J., & Trujillo, I. 2018, *Res. Notes Am. Astron. Soc.*, **2**, 144
- Roškar, R., Debattista, V. P., Stinson, G. S., et al. 2008, *ApJ*, **675**, L65
- Saintonge, A., & Spekkens, K. 2011, *ApJ*, **726**, 77
- Sandage, A., & Binggeli, B. 1984, *AJ*, **89**, 919
- Schaye, J. 2004, *ApJ*, **609**, 667
- Shen, S., Mo, H. J., White, S. D. M., et al. 2003, *MNRAS*, **343**, 978
- Shinn, J.-H. 2018, *ApJS*, **239**, 21
- Smithsonian Astrophysical Observatory, 2000, *SAOImage DS9: A utility for displaying astronomical images in the X11 window environment*, Astrophysics Source Code Library [record ascl:0003.002]
- Stone, C., Courteau, S., & Arora, N. 2021, *ApJ*, **912**, 41
- Taylor, M. B. 2005, *ASP Conf. Ser.*, **347**, 29
- Teeninga, P., Moschini, U. C., Trager, S., & Wilkinson, M. 2016, *Math. Morphol. Theory Appl.*, **1**, 100
- Toomre, A., & Toomre, J. 1972, *ApJ*, **178**, 623
- Trujillo, I., & Fliri, J. 2016, *ApJ*, **823**, 123
- Trujillo, I., Aguerri, J. A. L., Cepa, J., & Gutiérrez, C. M. 2001, *MNRAS*, **321**, 269
- Trujillo, I., Ferré-Mateu, A., Balcells, M., Vazdekis, A., & Sánchez-Blázquez, P. 2014, *ApJ*, **780**, L20
- Trujillo, I., Chamba, N., & Knapen, J. H. 2020, *MNRAS*, **493**, 87
- Trujillo, I., D'Onofrio, M., Zaritsky, D., et al. 2021, *A&A*, **654**, A40
- van der Kruit, P. C. 1979, *A&AS*, **38**, 15
- van der Kruit, P. C., & Freeman, K. C. 2011, *ARA&A*, **49**, 301
- van der Kruit, P. C., & Searle, L. 1981a, *A&A*, **95**, 105
- van der Kruit, P. C., & Searle, L. 1981b, *A&A*, **95**, 116
- Vazdekis, A., Ricciardelli, E., Cenarro, A. J., et al. 2012, *MNRAS*, **424**, 157
- Walt, S. v. d., Colbert, S. C., & Varoquaux, G. 2011, *Comput. Sci. Eng.*, **13**, 22
- Watkins, A. E., Salo, H., Laurikainen, E., et al. 2022, *A&A*, **660**, A69
- White, S. D. M., & Rees, M. J. 1978, *MNRAS*, **183**, 341
- York, D. G., Adelman, J., Anderson, J. E., Jr, et al. 2000, *AJ*, **120**, 1579
- Zhang, H.-X., Hunter, D. A., Elmegreen, B. G., Gao, Y., & Schruha, A. 2012, *AJ*, **143**, 47

Appendix A: Dealing with difficult cases

Until now, we consider that all the profiles visualised in Figs. 2, 4 and 3 have edges in their profiles. In this section, we show galaxies where the identification of the edge was less straightforward. We show three difficult cases in Fig. A.1 and describe each case below (galaxies ordered from left to right in the figure). These cases represent 10% of the cases which required more detailed analysis as described in our visualisation procedure (Fig. 1). The uncertainties quoted in the R_{edge} values were computed following the procedure described in Sect. 4.

- J004351.87+004807.05: While the edge is clearest in the μ_g and μ_r surface brightness profiles, two distinctive features appear in the $g-r$ and Σ_* profile: one at ~ 16 kpc and $\sim 21 \pm 3$ kpc. Upon examination of the 2D colour image, it is clear that the galaxy is not perfectly symmetric in the upper half. The first bump in the profile can thus be attributed to the edge in the upper half of the galaxy and the second to the outer marked edge. We prefer the outer feature as it is coincides with the change in slope visible in the surface brightness profiles.
- J233744.12+002127.92: μ_g and μ_r only show the break at ~ 30 kpc. However, the colour and mass density profile consist of an additional feature at 34 kpc and is marked as the edge here. Beyond this location the colour drops and rises again. The feature marked is preferred over that at 37 kpc where the colour rises because this does not correspond to a drop in mass density. The estimated uncertainty in the location of R_{edge} for this galaxy is ± 5 kpc.
- J012859.56-003342.96: This galaxy is an example with tidal-like features in its outskirts that break the elliptical symmetry of the main body as mentioned in Sect. 5 and Fig. 1. The change in slope is clearest in the $g-r$ colour profile where a drop towards bluer colours occur. In such cases, we think that the colour provides the best indication of the change in stellar properties that occur beyond the edge (see also the discussion in Trujillo et al. 2021).

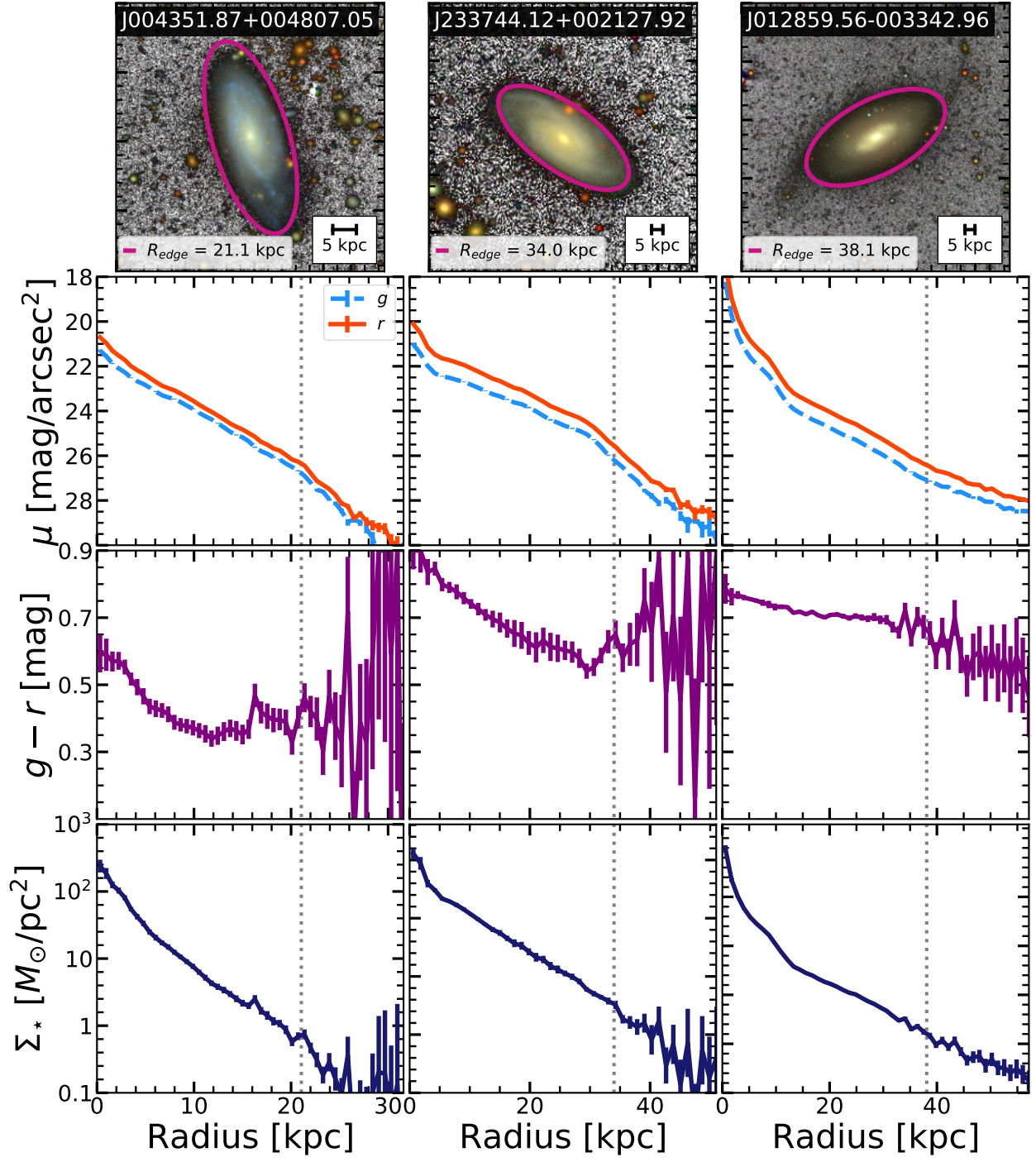


Fig. A.1. Radial profiles of three difficult cases. The panels are labelled as in Fig. 2.

Appendix B: The effect of image depth

We demonstrate that the criteria we have developed to locate the edges of galaxies (see Fig. 1) are not biased due to the depth of the IAC Stripe 82 images we used. The analysis presented herein is divided in two parts. In the first, we compare radial profiles at the depth of IAC Stripe 82 with those from the deeper LBT Imaging of Galactic Haloes and Tidal Structures (LIGHTS) Survey (see Trujillo et al. 2021, for more details) using g and

r -band images of a M33-like spiral galaxy, NGC 1042, as an example case. The images from LIGHTS are publicly available and have limiting depths in surface brightness of 31.2 and 30.5 mag/arcsec² (3σ , 10×10 arcsec²) in g and r respectively, with a pixel scale of 0.224 arcsec/pixel. In the second part of this appendix, we examine our capability of identifying the edges of galaxies in our parent sample by comparing the surface brightness at which they appear to the limiting surface brightness of the images IAC Stripe 82 used.

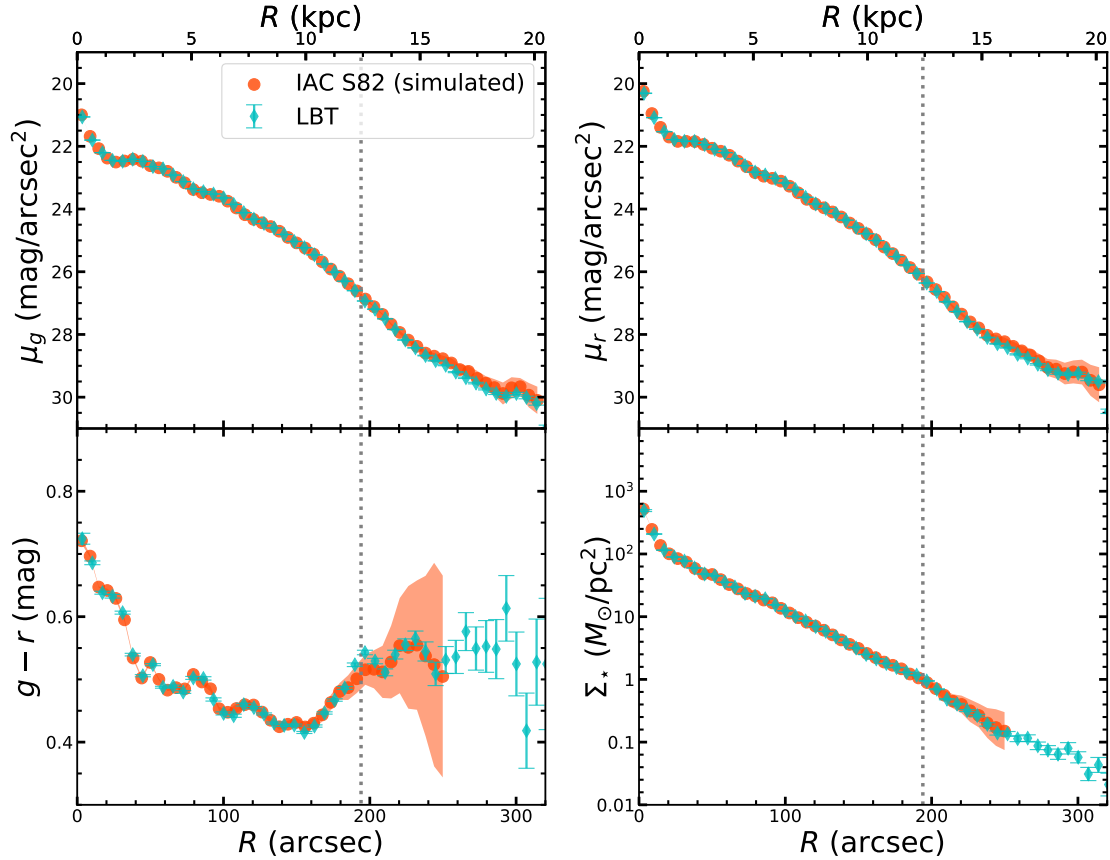


Fig. B.1. Radial profiles of NGC1042 from LBT (Trujillo et al. 2021) and simulated IAC Stripe 82 depth (this work, see text for details). The simulated profile is the median of 100 realisations and the shaded regions correspond to \pm three standard deviations up to where the deviation from the median is less than 0.2 mag. The vertical grey line is located at the edge of the galaxy ($R = 194''$).

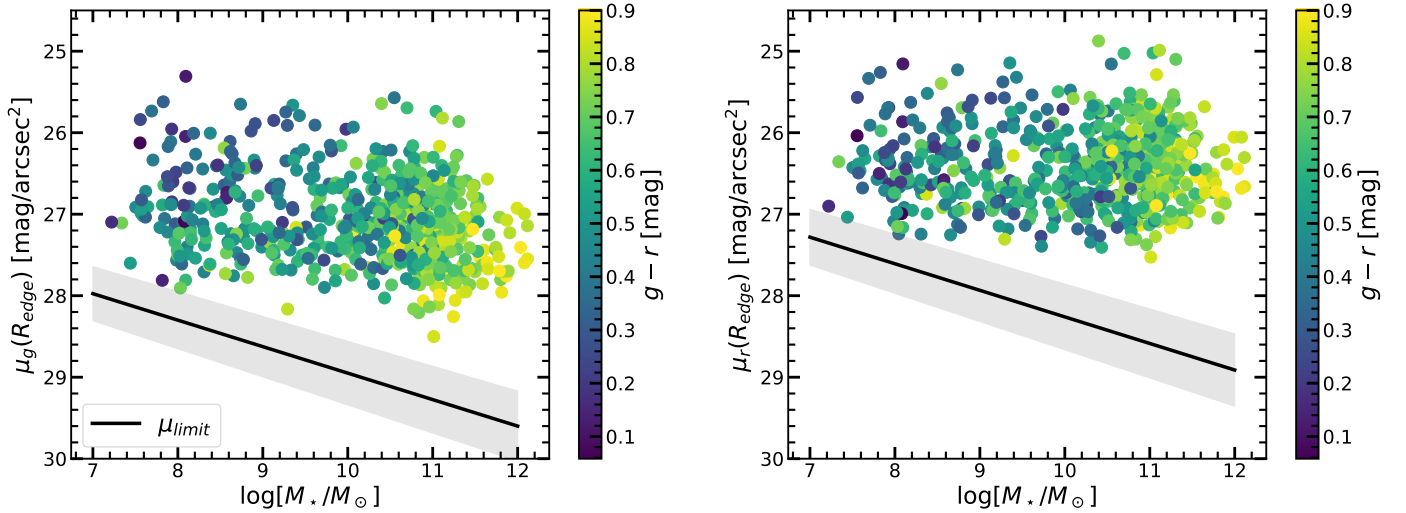


Fig. B.2. Observed surface brightness in the g (left) and r -band (right) at R_{edge} ($\mu_g(R_{\text{edge}})$ and $\mu_r(R_{\text{edge}})$ respectively) as a function of stellar mass. The edges appear well-within the 3σ limit of our data computed near R_{edge} (black line, see text for details).

B.1. LIGHTS vs. IAC Stripe 82

The LIGHTS data of NGC 1042 is interesting to explore for three reasons. Firstly, the LBT images are two magnitudes deeper than IAC Stripe 82 and consequently, compatible with the expected 10-year depth of the future LSST (in the r -band). This allows us to study the edge of a galaxy with a signal-to-noise more than five times higher than with IAC Stripe 82 imaging. Secondly, the edge of NGC1042 has been identified in Trujillo et al. (2021) and is one of the deepest observations of an edge to date for a nearby (13.5 Mpc; Monelli & Trujillo 2019) disk galaxy. Therefore studying the effect of depth in our procedure using these NGC1042 observations allow us to motivate future studies for similar galaxies. Lastly, NGC1042 has similar properties to the galaxy sample studied in P17 which we motivated earlier in Sect. 3. In other words, it is a disk galaxy with low inclination (axis ratio of 0.83) and given its distance, allows one to study its structure at a higher spatial resolution (65 pc/arcsec). All of the above reasons are well motivated for the goals of this and future work.

Unfortunately this galaxy is outside the footprint of Stripe 82. Therefore to study the effect of depth on the edge of NGC1042, we degraded the LIGHTS images to mimic IAC Stripe 82 in the following way. After background subtracting the LBT images (see Trujillo et al. 2021), we resampled them to match the SDSS pixel scale (0.396 arcsec/pixel) and zero point (22.5 mag), and added random gaussian noise to reach IAC Stripe 82 depth (see Sect. 3). In other words, we used the typical standard deviation of the background pixels in the LBT (σ_{LBT}) and IAC Stripe 82 (σ_{S82}) images based on their limiting depth to compute the required level of noise to degrade the LBT images (σ_{sim}):

$$\sigma_{\text{sim}}^2 = \sigma_{\text{S82}}^2 - \sigma_{\text{LBT}}^2. \quad (\text{B.1})$$

We then followed the procedure outlined in Fig. 1 on the ‘simulated’ IAC Stripe 82 images based on the degraded LBT images and locate the edge of the galaxy. For this particular galaxy, we followed the same masking procedure as that outlined in Trujillo et al. (2021) to ensure the same regions are compared when interpreting the data. The result is shown in Fig. B.1 where we show the radial profiles from LBT (taken from Trujillo et al. (2021)) and the median profile with simulated IAC

Stripe 82 depth after 100 separate realisations of random noise. The shaded regions correspond to \pm three standard deviations from the median profile plotted up to where the deviation is less than 0.2 mag. From the $g - r$ and Σ_* profile, we see that the location of the edge ($R = 194''$ marked with the vertical dotted line) does not change between the profiles. The main difference is that the profiles are more noisier in the outskirts with IAC Stripe 82 depth but this does not prevent the identification of the edge (although it is certainly harder) using our criteria. For NGC1042, the edge appears at a mass density of $1 \text{ } M_{\odot}/\text{pc}^2$.

B.2. Detecting edges with IAC Stripe 82 depth

In the second part of this appendix, we compare the surface brightness at which the edges of our parent sample appear with the limiting surface brightness of the IAC Stripe 82 images used. We do this by computing the representative depth of each image as it depends on the size of galaxies (i.e. the area near R_{edge} for each galaxy). This can be understood in the following way. In general, the limiting surface brightness of an image can be computed as the $x\sigma$ fluctuation (where x corresponds to the number of deviations) with respect to the background of the image that is measured over an area A . The form ($x\sigma; A \text{ arcsec}^2$) is called a metric. As a rule of thumb, A is optimally chosen according to the apparent size of objects under consideration (using a circle, box etc.). For example in the SDSS g -band, we may write that the limiting surface brightness depth is $\mu_{\text{lim},g} \sim 26.5 \text{ mag/arcsec}^2$ ($3\sigma; R = 12''$), where A was chosen to be the area of a circle with radius $R = 12$ (Kniazev et al. 2004). This is a reasonable choice for A because Kniazev et al. (2004) was interested in the search for new dwarf and low surface brightness galaxies in SDSS. To convert the limiting surface brightness (at a given wavelength λ) from metric ($x_1\sigma; A_1$) to ($x_2\sigma; A_2$) is:

$$\mu_{\text{lim},\lambda}(x_2\sigma; A_2) = \mu_{\text{lim},\lambda}(x_1\sigma; A_1) - 2.5 \log \left[\frac{x_2}{x_1} \right] + 2.5 \log \left[\frac{A_2}{A_1} \right]^{1/2}, \quad (\text{B.2})$$

where x_k is the number of variations σ and A_k is the area used for $k = 1, 2$. Given that we know the depth of our images for an area of $10 \times 10 \text{ arcsec}^2$ (Sect. 3), we can use Eq. B.2 to compute the limit over different areas. We do this for the size of

each galaxy in our parent sample in the following way to confirm that the depth of the image is enough to detect their edges.

We plot the observed surface brightness in the g -band at which the edges of the galaxies appear ($\mu_g(R_{\text{edge}})$) as a function of stellar mass in Fig. B.2. To determine the representative limit of the data given the size of the galaxy, we compute the 3σ limit over the area of pixels in an elliptical annuli (used when deriving the surface brightness profile, see Sect. 4) at R_{edge} for each galaxy. The line of best fit is plotted in black and the grey shaded region bounds the $\pm 1\sigma$ dispersion of the fit.

The figure shows that all the edges appear at surface brightnesses above the limit near R_{edge} , even for the redder galaxies. Therefore, we may conclude that the edges we study here are not a consequence of image depth and the stratification in the size–stellar mass plane is not an observational bias towards bluer edges. In other words, if there were larger galaxies with redder edges in our sample at any fixed stellar mass, we should have been capable of identifying them with our data.

Appendix C: The dependence of radial profile derivation methods on galaxy orientation

Two methods have been mainly used to derive the radial profiles of galaxies in the literature. In the first method, radial profiles are derived along the galaxy’s semi-major axis using a slit of fixed width⁹. The second method uses elliptical annuli: the axis ratio and position angle to parameterise the ellipse for this procedure may either be fixed (this work) or allowed to vary along the main body of the galaxy. The slit method is generally used to characterise the radial profiles of edge-on oriented galaxies as the method is limited to imaging with high signal-to-noise and edge-on galaxies are naturally observed deeper than face-on ones due to the line-of-sight integration. On the other hand, the ellipse method is limited to galaxies that can be described by an ellipse and this is not the case for edge-on or near edge-on ($q \lesssim 0.3$) galaxies with prominent bulges. Therefore, the ellipse method has been used to derive the profiles of low-inclination galaxies and is possible with lower signal-to-noise imaging.

In this appendix, we study and compare both of these profile derivation methods on an edge-on and low-inclination galaxy to examine its effect on the visibility of the edge and on galaxy orientation. We make use of the LBT data of the low-inclination galaxy NGC1042 as in Appendix B.1 and SDSS DR12 images of the edge-on galaxy UGC09138 shown in Fig. 2.

For the slit method, we used a 1.2 kpc width for both galaxies and we followed the procedure outlined in Sect. 4 for the elliptical annuli method. The result of the comparison is shown in Fig. C.1 for UGC09138 (top panels) and NGC1042 (lower panels). The profiles derived using the slit method is plotted in solid, cyan lines and ellipse method in dashed, black ones. It can be seen that the edge of UGC09138 may only be located using the slit (semi-major) axis method in the μ_g and Σ_* profiles while both methods may be used to locate the edge of NGC1042 in the Σ_* profile. However, the edge also becomes clearer in the μ_g profile of NGC1042 using the slit method. The latter result thus highlights the fact that deeper imaging with higher signal-to-noise than SDSS or IAC Stripe 82 such as LIGHTS and the future LSST will allow the identification and characterisation

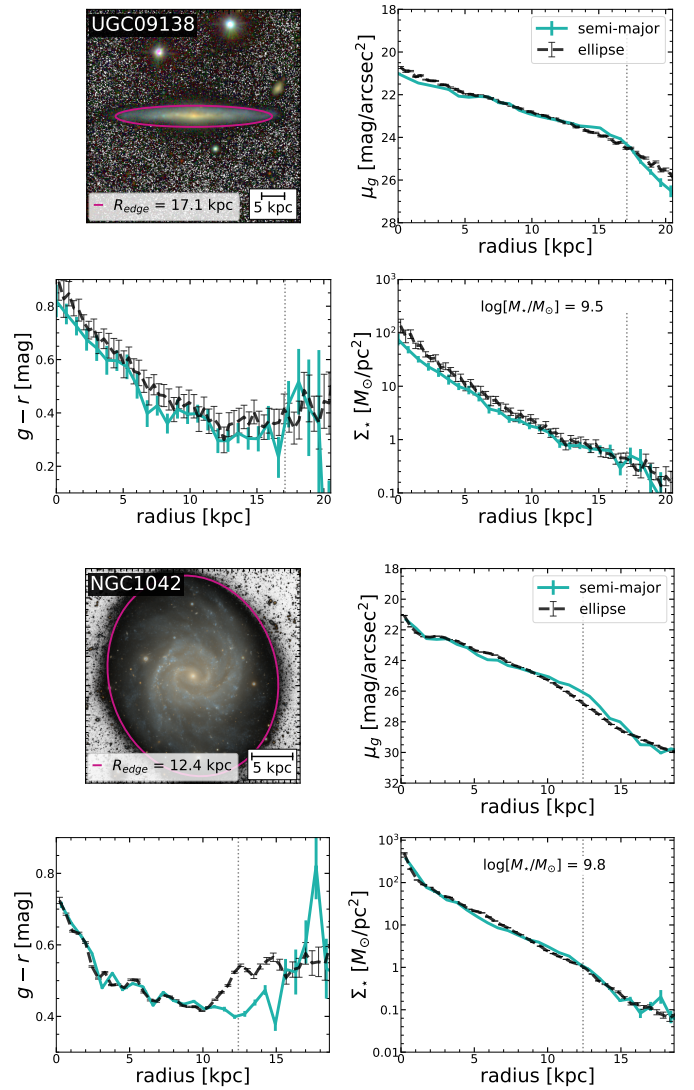


Fig. C.1. Comparison between radial profiles derived using a 1.2 kpc slit through the semi-major axis of the galaxy (solid, cyan) and elliptical annuli (dashed, black) for UGC09138 (edge-on, top panels) and NGC1042 (low-inclination, lower panels). The elliptical annuli method is suitable for the low-inclination galaxies studied in this work. See text for details.

of edges using the slit method also for near face-on ($q \geq 0.8$) galaxies.

C.1. Dwarf galaxy SDSS J224114.29-003710.2

We have identified R_{edge} using the change in slope in the stellar mass density profile of the dwarf galaxy SDSS J224114.29-003710.2 in Fig. 4. The profiles plotted in that figure were derived using the ellipse method as described above and in Sect. 4. As an example, we also derive the profiles using the slit method, with a 1 kpc width slit through the semi-major axis of the galaxy. The profiles from the two methods are compared in Fig. C.2. We mark R_{edge} as in Fig. C.1 and confirm that both methods have a signature of the edge in the same location. However, while the slit method additionally provides the signature in the $g-r$ profile as a sharp drop towards bluer outskirts, we point out that this feature does not take into account the global colour of the galaxy at R_{edge} because it was strictly computed within the slit region.

⁹ A slightly different approach to this method is the use of a wedge shape (see Stone et al. 2021).

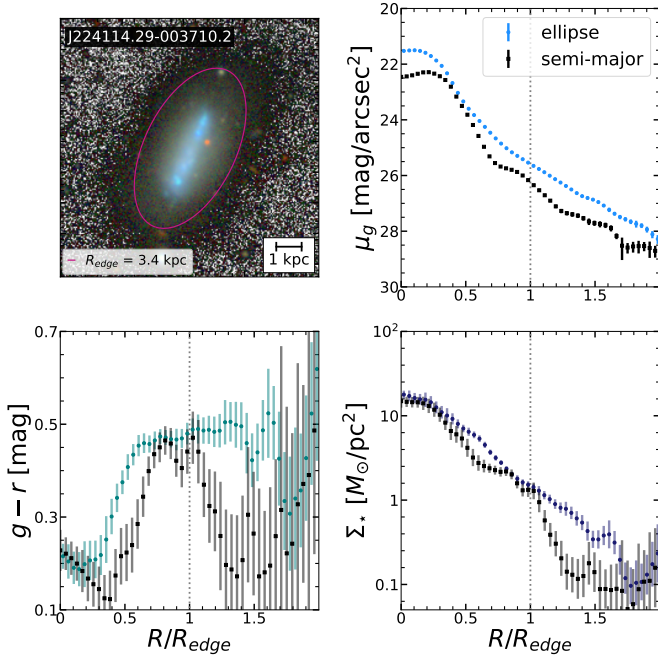


Fig. C.2. Comparison between radial profiles derived for the dwarf galaxy SDSS J224114.29-003710.2 using a 1 kpc slit through its semi-major axis (squares, black) and elliptical annuli (dotted, blue). The x -axis and R_{edge} for this galaxy are scaled and marked similarly to Fig. 4.

Appendix D: Fits to the $\Sigma_*(R_{\text{edge}}) - M_*$ relation

In this appendix, we justify the use of Eqs. 3 and 4 as best fits to the $\Sigma(R_{\text{edge}}) - M_*$ relation shown in Fig. 5.

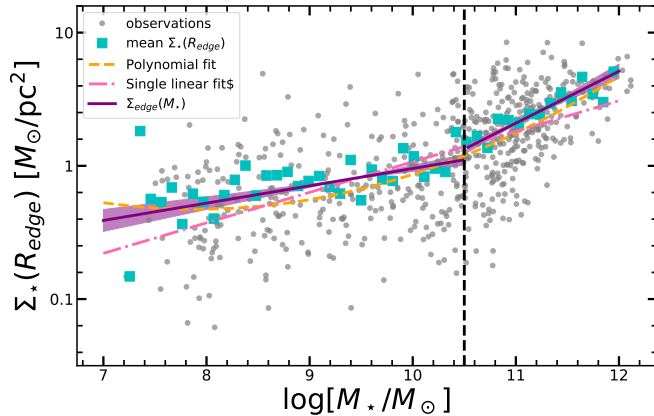


Fig. D.1. Fitting functions for the $\Sigma_*(R_{\text{edge}}) - M_*$ relation (grey points). The mean $\Sigma_*(R_{\text{edge}})$ is computed in steps of 0.1 dex over the plotted stellar mass range (cyan squares). The best fits (purple lines) are the two linear relations in Eqs. 3 and 4, split at $10^{10.5} M_\odot$ (vertical black dashed line). For contrast, we also show a single linear fit (pink dot-dashed line) and polynomial fit of degree two for the full sample (orange dashed line).

In Fig. D.1, we compare fitting the measurements using two linear fits (as adopted in this work) with a single linear relation and a polynomial of degree 2. We test whether these fitted relations pass through the mean $\Sigma_*(R_{\text{edge}})$ in steps of 0.1 dex over our full stellar mass range ($10^7 M_\odot < M_* < 10^{12} M_\odot$). The grey points show our measurements (Fig. 5), the cyan squares show the mean $\Sigma_*(R_{\text{edge}})$ in each stellar mass bin, the pink dot-dashed

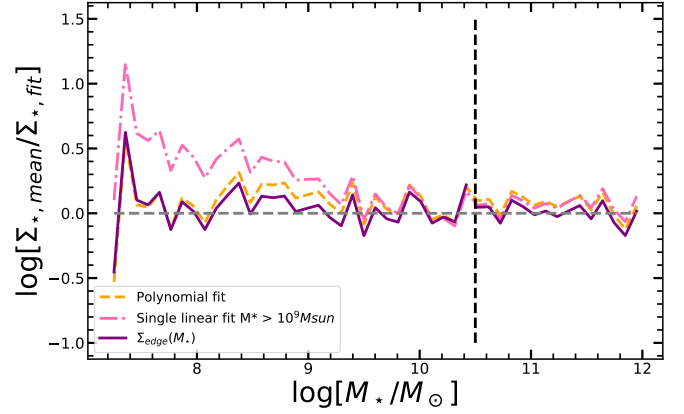


Fig. D.2. Comparing the residuals of the fits to the mean $\Sigma_*(R_{\text{edge}})$ relation. The single linear fit in pink used here is computed for galaxies with $M_* > 10^9 M_\odot$. The reduced chi-square values are 1.6 and 1.7 for the purple $\Sigma_{\text{edge}}(M_*)$ relations in Eqs. 3 and 4, 3.1 for the pink linear relation and 2.9 for the polynomial fit.

line shows the single linear fit, the orange dashed line shows the polynomial fit of degree 2 and the purple lines show the linear relationships split at the stellar mass of $10^{10.5} M_\odot$ (Eqs. 3 and 4). We mark where the relations split with a vertical dashed black line. The shaded region shows the 1 sigma scatter in the fitted linear relations.

From this figure, it is clear that both the single linear and polynomial fits do not pass through all the mean points (cyan) of the $\Sigma_*(R_{\text{edge}})$ –stellar mass plane. The relation also changes slope at a stellar mass of $10^{10.5} M_\odot$ (vertical dashed line). These findings do not change if we restrict the single linear fit to galaxies only with stellar masses $M_* > 10^9 M_\odot$, which we confirm by studying the residuals of the fits with respect to the mean data points shown in Fig. D.2. The reduced chi-square values are 1.6 and 1.7 for the purple $\Sigma_{\text{edge}}(M_*)$ relations in Eqs. 3 and 4, 3.1 for the pink linear relation and 2.9 for the polynomial fit, with respect to the mean data points.

We also confirm that these results do not change if we exclude the dwarf galaxies in our sample. Therefore, we use the two linear relations as the best fits to our measurements in the $\Sigma_*(R_{\text{edge}})$ –stellar mass plane. This choice also leads to comparable sample sizes of galaxies with stellar masses either greater or less than $10^{10.5} M_\odot$.

Finally, for the late-type galaxies plotted in Fig. 8, we point out that while the scatter of the relation is large, the Spearman's correlation coefficient is positive and with a p -value $< 1\%$. This result is an indication that there is a very strong relation in this parameter space even though the scatter is high.

Appendix E: The usability of R_{edge} in large-scale, multi-band surveys

We have visually identified the edges of a large sample of galaxies (645 galaxies). Such a detailed study will no longer be feasible once data will be acquired from wide surveys such as the LSST mentioned above, which is expected to provide 20 TB of data per night¹⁰. A natural question is thus how convenient and usable is R_{edge} as a size measure to be included in large-scale galaxy catalogues?

We emphasise that we use the stellar mass density at the location of the edge as a *proxy* for the underlying theoretic-

¹⁰ <https://www.lsst.org/scientists/keynumbers>

cal gas density threshold required for star formation in galaxies (see Schaye 2004; Trujillo et al. 2020). For this reason, as an exercise, we used the $\langle \Sigma_{\text{edge}}(M_*) \rangle$ relations (Eqs. 3 and 4) to ascertain the average location of the edge for each galaxy, $\langle R_{\text{edge}} \rangle$. For each galaxy with stellar mass M_* we locate the position of $\langle \Sigma_*(R_{\text{edge}}) \rangle$ using the stellar mass density profile of the object: $\Sigma_*(\langle R_{\text{edge}} \rangle) = \langle \Sigma_{\text{edge}}(M_*) \rangle$. The resulting $\langle R_{\text{edge}} \rangle$ –stellar mass relation for the parent sample is shown in Fig. E.1. The $\langle R_{\text{edge}} \rangle$ –stellar mass plane also follows a power law of the form $\langle R_{\text{edge}} \rangle \propto M_*^{\langle \beta \rangle}$. As expected, the dispersion of this plane is less than that of the observed R_{edge} –stellar mass plane: $\sigma_{\langle R_{\text{edge}} \rangle} = 0.093 \pm 0.005$ dex but the slope is compatible $\langle \beta \rangle = 0.30 \pm 0.006$.

The above result suggests that Eqs. 3 and 4 could potentially be used to obtain $\langle R_{\text{edge}} \rangle$ and provide a proxy for the size of any galaxy, provided its stellar mass is known. These laws can be useful for larger galaxy samples and automated cataloguing in future multi-band surveys such as the LSST. Providing $\langle R_{\text{edge}} \rangle$ is also advantageous for cases where the edge is not apparent and thus serves as a prediction of where the edge should be for a given galaxy. Strong deviations from this prediction could then provide insights about the stellar population properties in the outskirts of the galaxy in comparison with the parent population.

We point out that galaxies with low stellar density and mass (i.e. low surface brightness galaxies, e.g. Sandage & Binggeli (1984)) are not included in our sample and the validity of Eqs. 3

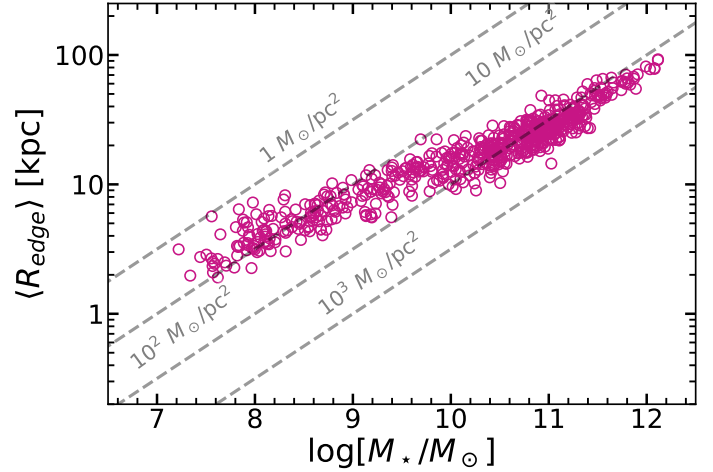


Fig. E.1. $\langle R_{\text{edge}} \rangle$ –stellar mass relation for the parent sample resulting from the density threshold laws in Eqs. 3 and 4. The structure of the relation is almost exactly the same as the observed R_{edge} –stellar mass relation shown in Fig. 5 which makes it a promising method to determine a proximal measure of R_{edge} automatically for large-scale cataloguing.

and 4 to such galaxies need to be investigated in future work (but see Chamba et al. 2020).